THESIS FOR THE DEGREE OF DOCTOR OF PHILOSOPHY

Laser-based powder bed fusion of stainless steels

Powder properties, processability and microstructure

DMITRI RIABOV

Department of Industrial and Materials Science

CHALMERS UNIVERSITY OF TECHNOLOGY

Gothenburg, Sweden 2022

Laser-based powder bed fusion of stainless steels
Powder properties, processability and microstructure

DMITRI RIABOV
Department of Industrial and Materials Science
Chalmers University of Technology

Abstract

The aim of the present work has been to widen the knowledge of how variations within powder manufacturing affect laser-based powder bed fusion processing, and how this processing affects the microstructure and strength of stainless steels. The approach was to keep the processing parameters fixed while the powder feedstock was varied. This methodology enabled an isolation of the powder properties, which were correlated to the residual porosity in the printed samples. After establishing the relationship between printability and powder properties, a careful microstructural investigation was performed to understand what features are responsible for the relatively high strength of austenitic stainless steels. Two different alloying strategies were attempted to boost the strength further, introducing additional oxygen into the processing chamber for an in-situ synthesis of nanometric oxides, and designing a composition that produces strengthening precipitates upon aging.

The initial powder investigations revealed that 316L powder produced using vacuum induction melting inert gas atomization (VIGA) and conventional gas atomization (CGA) displayed similar oxidation states despite different atomization gases. The use of water in the atomization process however changed the oxidation state significantly, resulting in more extensive formation of oxide particulates on the powder surfaces. Analysis of the powder properties showed similar trends as the surface analysis, where the VIGA and CGA powder grades had similar flow properties. While water atomized (WA) powder had significantly lower flowability as compared to the other tested grades. The lower flowability caused a significant increase in residual porosity when printing with layer thicknesses above 20 μm.

Microstructural characterization of printed 316L specimens revealed a hierarchal structure consisting of elongated grains and within them a fine cellular structure. The cell structure was found to act as soft grain boundaries, hence strengthening the material without sacrificing ductility too much. This structure was found to be stable up to 800 °C.

Conceptually, the in-situ synthesis of finely distributed nanometric oxides using water atomized powder was shown to work. However, the size and number densities of the oxides must be further optimized to provide a strengthening effect. Another strategy for increasing the strength was by developing a heat-treatable composition using thermodynamic simulations. This resulted in the development of a novel stainless tool-steel composition. This new material had excellent printability with a fully martensitic structure in the as-printed condition and possessed a yield strength of nearly 1600 MPa after aging. The precipitates were found to have relatively slow coarsening rates and therefore the material retained much of its hardness despite long aging times.

Keywords: additive; PBF-LB; powder; flowability; spreadability; surface; oxidation; morphology; 316L, maraging; precipitates; oxides; ODS; atomization; mechanical properties.

Preface

The work presented in this doctoral thesis was conducted at the Department of Industrial and Materials Science and the Department of Customization Technologies in Höganäs between May 2017 and September 2022. The work was conducted in the framework of the Center for Additive Manufacturing – Metal (CAM^2), supported by Vinnova, as an industrial PhD project that was financially supported by Höganäs AB. The research was conducted under the supervision of Adj. Prof. Sven Bengtsson at Höganäs AB and Prof. Eduard Hryha at Chalmers. Prof. Lars Nyborg acted as examiner and co-supervisor.

The thesis consists of an introduction followed by the appended papers as listed below:

List of appended papers

I. **Effect of atomization on surface oxide composition in 316L stainless steel powders for additive manufacturing**
D. Riabov, E. Hryha, M. Rashidi, S. Bengtsson and L. Nyborg
Surface and Interface Analysis 52 (2020) 694-706
DOI: 10.1002/sia.6846

II. **Effect of powder variability on laser powder bed fusion processing and properties of 316L**
D. Riabov, L. Cordova, E. Hryha and S. Bengtsson
European Journal of Materials (2022)
DOI: 10.1080/26889277.2022.2064772

III. **Investigation of the strengthening mechanism in 316L stainless steel produced with laser powder bed fusion**
D. Riabov, A. Leicht, J. Ahlström and E. Hryha
Materials Science and Engineering: A 822 (2021) 141699
DOI: 10.1016/j.msea.2021.141699

IV. **Effect of the powder feedstock on the oxide dispersion strengthening of 316L stainless steel produced by laser powder bed fusion**
D. Riabov, M. Rashidi, E. Hryha and S. Bengtsson
Materials Characterization 169 (2020) 110582
DOI: 10.1016/j.matchar.2020.110582

V. **Design and characterization of a cobalt-free stainless maraging steel for laser-based powder bed fusion**
D. Riabov, K. Frisk, M. Thuvander, E. Hryha and S. Bengtsson
Submitted for publication

Contribution to the appended papers

I. The author planned and executed most of the experimental work. M. Rashidi performed the lift-out of the TEM sample. Parts of the analysis were made in collaboration with the co-authors. The writing was in collaboration with the co-authors.

II. The author planned and executed the experimental work and wrote the paper in collaboration with the co-authors.

III. The author performed the tensile testing and transmission electron microscopy work. The EBSD measurements were performed by A. Leicht. The author analyzed the results and wrote the paper in collaboration with the co-authors.

IV. The author planned and executed the experimental work together with the co-authors. The author analyzed the results and wrote the paper in collaboration with the co-authors.

V. The author planned and executed the printing, mechanical evaluations and TEM investigations. Thermodynamic simulations were performed by K. Frisk. APT investigations and analysis were performed by M. Thuvander. The manuscript was written in collaboration with the co-authors.

Papers not appended in this thesis

A. Factors affecting printability of 316L powders using the DMLS process
D. Riabov and S. Bengtsson
Conference proceeding of WorldPM 2018, Beijing, China

B. Metal Powder Production for Additive Manufacturing
E. Hryha and D. Riabov
Encyclopedia of Materials: Metals and Alloys, vol. 3, pp. 264-271. Oxford: Elsevier

Table of contents

1. Introduction

Additive manufacturing (AM) primarily evolved in sectors with high demands on part complexity and short lead times. Typically, such sectors are the medical, aerospace and energy industries. They all have strict requirements on material performance, such as strength at elevated temperatures, biocompatibility and corrosion resistance. Additionally, they tend to have relatively short production runs and low cost-sensitivity, hence allowing comparably costly production routes such as AM.

There are numerous technologies within the collective term of AM, but a common denominator is the layer-by-layer process by which a part is built. According to the 2022 report of AMPOWER [1] the largest metal AM technology in 2021 was laser-based powder bed fusion (PBF-LB). PBF-LB uses metal powder as its feedstock material that is selectively melted using a focused high-intensity laser beam. Metal powder is commonly produced through atomization, a process where a liquid is finely dispersed into droplets that solidify into fine powder. This powder is produced mainly by inert gas atomization, allowing complex alloys to be atomized. Inert-gas atomization is, however, not the only way to produce suitable powder for PBF-LB.

Many technologies are at their early stages cost inefficient, an example is silicon solar cells that started off at nearly 1000 EUR/W in 1975 and dropped to below 1 EUR/W in 2015 [2]. In the current state, metal powder constitutes a small fraction of the total part cost of the PBF-LB process [1]. However, if the PBF-LB technology follows a similar cost-path as solar cells did, metal powder will become a more significant part of the processing cost. Then cost-efficient metal powder grades can become vital for increasing the utilization of the PBF-LB market.

Cost-efficient powder grades can be made by altering the atomization process, which will influence the powder properties. These property changes include the oxidation state of the powder surface, powder morphology and powder rheology, which can influence the printability of the powder. To facilitate the introduction of cost-efficient powder grades to AM, the fundamental relationship between powder properties and part integrity needs to be clarified. Only then will it be possible to identify to what extent cost-efficient metal powder grades can be used in AM, including their opportunities and limitations relative to the industry standard powder grades.

The AMPOWER report also mentions the popularity of stainless steels for AM [1], sharing the second place with Ni-based alloys to Ti-based alloys. PBF-LB processing of stainless steels, apart from having a considerably large processing window, has shown to boost their strength significantly – to a point where they can be considered for structural applications. Hierarchical microstructural features stemming from the rapid solidification process have been reported to be responsible for the observed high strength [3]. This opens for further questions whether PBF-LB processing can be exploited to further increase the mechanical performance of stainless steels, either through tailoring of the processing parameters or through clever alloying modifications.

1.1 Research objectives

The objectives of this study have been to advance the understanding of how different atomization processes affect the powder and its PBF-LB processing, to further clarify the strengthening mechanisms of PBF-LB processed stainless steels, and to depict possible strategies of increasing the strength of these alloys. These objectives can be summarized in the following research questions (RQ):

RQ 1.   How do different atomization practices affect the powder properties and their processability by means of PBF-LB?

RQ 2.   What are the strengthening mechanisms of PBF-LB processed stainless steels?

RQ 3.   How can the strength of stainless steels be increased without compromising processability?

1.2 Research approach

This work aims to deepen the knowledge of the influence of the atomization process on the resulting powder properties, their effect on PBF-LB processability and finally, the relationship between microstructure and mechanical performance of stainless steels. For clarity, the research efforts were divided into two parts, one dealing with powder (RQ1) and one dealing with the microstructure and properties of stainless steels (RQ2 and RQ3). A schematic of the approach can be seen in Figure 1.
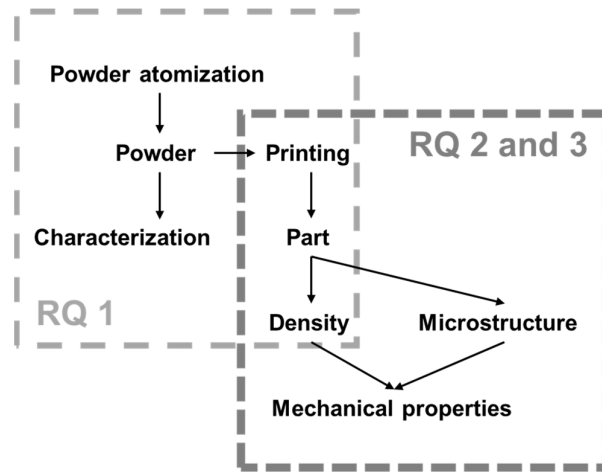
Figure 1. Schematic of the research approach. The topics covered in the various RQ are highlighted.

The first RQ can be divided into two sub-topics, one that deals with specifically how atomization media affect the powder surface and its oxidation and another one that deals with the physical powder properties and how these affect the printability (sample reaching high densities during PBF-LB processing). The first part of RQ 1, *Paper I*, addressed three 316L powder grades that were atomized with Ar, N_2 and H_2O. The second part of RQ 1, *Paper II*, investigated these powder grades but with a focus on the physical powder properties characterized using both conventional and new methodologies, including a powder rheometer and a revolving drum analyzer. In *Paper II*, the investigated powder grades were also processed

by PBF-LB, and the resulting porosity of as-built material was correlated to the powder properties.

The aim of the first part dealing with RQ1 was hence to provide a benchmark of the powder quality and performance relative to the industry standard powder grades. Another aim was to explore possibilities and limitations of emerging powder characterization methods. Generally, the approach was to characterize, print and identify outputs that are relevant for PBF-LB processing.

The second part (RQ2 and RQ3) consisted of identifying the microstructure that is responsible for the relatively high strength in austenitic stainless steels built using PBF-LB. Like the first part, this can be further divided into two topics: one that defines the baseline PBF-LB microstructure of 316L stainless steel and how it resists deformation, *Paper III*; another one addressing methods of increasing the strength of stainless steels, *Paper IV* and *Paper V*.

The aim of this second part was to gain a fundamental understanding of how PBF-LB processed microstructures are strengthened. This was done so that strategies of increasing the strength further could be explored, either by exploiting PBF-LB processing or by adjusting the powder chemistry.

2. Metal additive manufacturing

Additive manufacturing has over the past decade experienced a boom in public interest, scientific advances, and industrialization. This trend can clearly be seen in the number of annually published articles and Google searches on additive manufacturing, as seen in Figure 2.
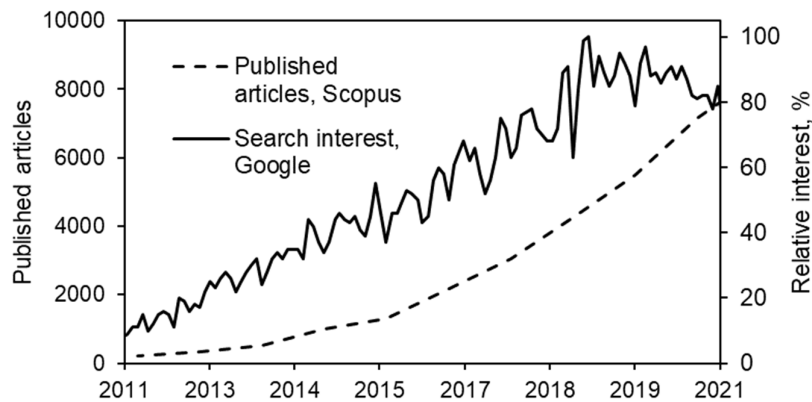
Figure 2. Annually published articles according to Scopus and relative interest according to Google for the search term "additive manufacturing" from 2011-2021. The search was conducted June 2022.

A New York Times article from 2010 called 3D printing, or AM, a manufacturing revolution [4]. More than 10 years later, conventional manufacturing is still vastly dominating. Despite this, AM is beginning to compete with conventional processes where there is a need for high part complexity, often in combination with fast turn-around times. One of the first major industrial applications of AM in Sweden was by Siemens Energy AB that used these two advantages of AM to repair burner nozzles, found in industrial gas turbines. This implementation greatly reduced the lead-time. The success pushed Siemens Energy AB to re-design the burner so that it could be completely manufactured using AM – resulting in a 13-part integration while also improving the performance [5], [6].

Another successful application of metal AM is within the dental and orthopedic industries. These parts are typically complex and have limited production numbers, thus making them ideal for AM, which also enables the possibility to produce patient specific implants. In a recent review by Palmquist et al. [7] the use AM produced implants were shown to have several merits over conventionally manufactured implants. These included the possibility to create lattice structures in AM hence reducing the stiffness mismatch between implant and bone, and the micro-porous geometry improved bone ingrowth [7].

It can be seen from the two mentioned examples that AM shines in applications where there is a need for geometrical complexity that is difficult to produce by other means, and where the number of produced parts is limited. It is therefore also heavy employed in the production of functional prototypes.

Additive manufacturing is, as the name suggests, a process where material is constantly added as opposed to being removed to produce a final component geometry. This additive process on a first glance seems easy – yet is more complex when considering the material supply and how

5

the added material is fused together. The feedstock material must be able to be supplied to the process while also being able to form delicate features of the part. For example, the use of powder as compared to wire. Powder can flow into confined spaces such as thin layers, hence forming delicate details, while a wire can be supplied at faster rates but at a diminishing resolution. This is what sets the different AM technologies apart, some use wire or powder as the feedstock material, and fused either through melting by using high-powered beams or by means of sintering at high temperatures. According to the recently issued ASTM/ISO 52900:2021 standard there are seven main AM technologies [8], out of which three use metal powder as the feedstock material. They are listed below:

- Binder jetting (BJT)
- Directed energy deposition (DED)
- Powder bed fusion (PBF)

Out of the three, PBF has been the focus of this work. However, there is some overlap in the powder chemistry and powder size between these technologies, hence some of the findings in this work can be applicable to the other AM technologies. PBF has two sub-technologies that are defined according to their beam type, either laser-based and hence the name PBF-LB or electron-based (PBF-EB).

2.1 Powder bed fusion

Figure 3 presents a schematic of the PBF system, in this case specifically a PBF-LB system. The systems, apart from the beam source with its associated beam deflection system, generally consist of a powder dispenser, a powder recoating system that supplies the powder to the build platform, and an overflow bin for excess powder. Also, there is a system that controls the atmospheric condition within the build chamber as to prevent oxidation during the building process. Lastly, there can be a monitoring system that logs various parameters and the printing process.

The principal difference between LB and EB systems is the use of a laser beam as compared to an electron beam. With the LBF-EB systems the beam deflection occurs through magnetic lenses, similar to the scanning electron microscope (SEM) as described in section 6.4.1. As there are no moving parts in the magnetic lenses the beam deflection speed can be much higher in PBF-EB systems as opposed to the PBF-LB systems – resulting in typically higher attainable build rates in PBF-EB. To reduce the interaction of the electron beam with the atmosphere, the PBF-EB systems are pumped down to vacuum during the printing process, as opposed to the laser systems that are run at inert atmospheric conditions and continuously flushed with inert gas, typically argon.
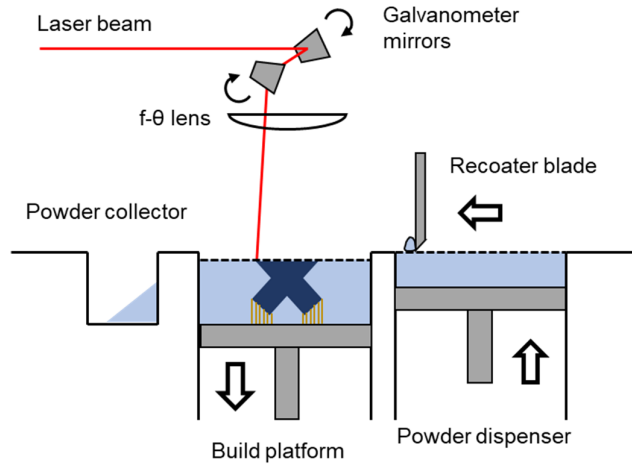
Figure 3. A schematic of the various components of a PBF-LB system.

The PBF workflow begins with the part design. The design is created digitally using computer-aided-design (CAD) software, this results in a 3D-model of the design with all the dimensional information incorporated into it. This design-file, or CAD-file, is converted into an STL-file, an acronym for stereolithography, which is commonly used also in computer-aided manufacturing (CAM). The STL-file transforms the design into triangulated surface, consisting of many small triangles, that closely approximates the CAD-design. This ensures consistency between different CAD software prior to importing the file into an AM software. Within the AM-software it is possible to re-orient the designed part within the virtual build volume, to generate support structures that anchor the design to the build platform, and to define the process parameters. The AM software then sends the file including all printing information to the AM machine and its print program.

Once the file is transferred the printing preparations can be made. The preparations consist of loading the powder into the machine, inserting and leveling the build-plate, and applying the first powder layer onto the build plate. The machine then purges the atmosphere inside of the build chamber and starts melting the powder according to the pre-defined geometry for the layer in question. After each exposure, the powder dispensing platform is raised the required distance for full powder coverage and the re-coater blade rakes the powder over the build plate. Debris and surplus powder end up in the powder collecting bin. This iterates till the print is completed.

After the print is finished, powder is recovered through a vacuum system and the build-plate is recovered. The used powder is sieved to remove coarse process by-products before it can be used again. Finally, the build-plate is post-processed, which includes heat-treatment, part-removal, and final machining. Heat-treatment can be done both prior to sectioning and after sectioning.

When it comes to powder for the two systems, there are some differences between the required powder properties of the two beam types. Powder for LBF-EB is usually supplied in the 40 to 100 μm range – allowing for a higher utilization of the atomized powder. However, the use of this relatively coarse powder has a significant influence on the surface quality of parts produced with PBF-EB [9]. The use of finer powder sizes can lead to a phenomenon called *smoking* in PBF-EB, which limits the use of it for EB systems. Smoking occurs when the powder particles

act as insulators rather than conductors, leading to charging of the powder rather than melting. This causes the powder particles to disperse from the powder bed – forming a smoke-like cloud. An example of this phenomenon can be seen below in Figure 4. Another reason for smoking can be excessive surface powder oxidation, as a thick oxide layer can act as an insulator. Therefore, some cleanliness requirements for powder PBF-EB can be of practical significance [10]. As LB systems do not suffer from problems associated with charging, it is possible to use finer powder factions. This enables printing with thinner layer thicknesses hence achieving better print resolution and surface quality. Therefore, PBF-LB systems use powder in the range of between 10 and 60 μm. However, too fine powder can cause issues with spreadability as inter-particle forces increase with decreasing particle size.
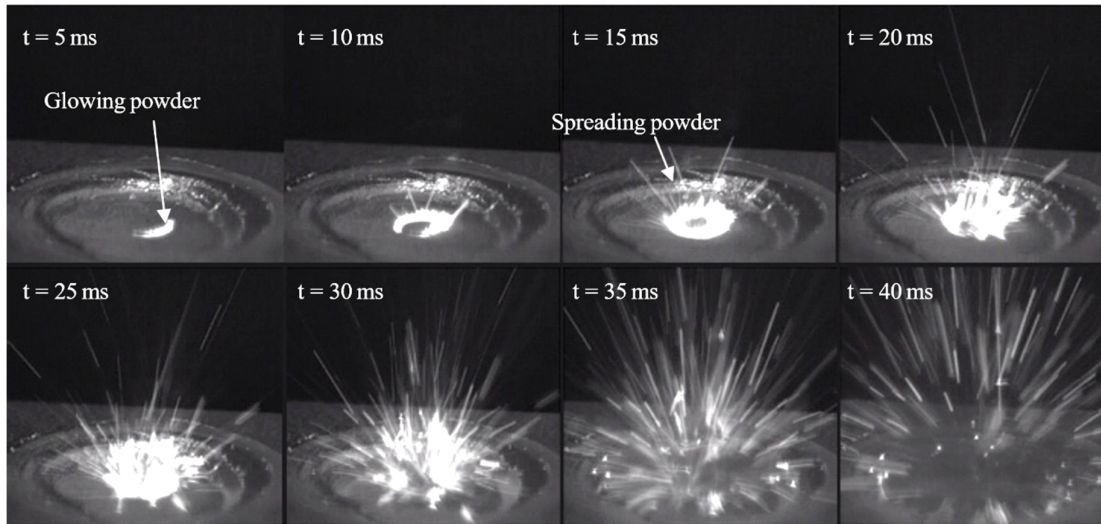

Figure 4. A sequence leading up to a smoke-event in EB-PBF. Reproduced with permission from Springer Nature [11].

2.2 Considerations specific for PBF-LB

2.2.1 Scanning strategy and parameters

An important part of any additive technology is the development and optimization of printing strategies and its associated parameters, as these will largely determine the quality and final properties of the additively manufactured part. As such, many PBF-LB system suppliers consider these strategies and parameters as their intellectual property and are therefore hidden from the operator. The scanning strategy is defined according to the laser exposure sequence and depending on the layer and part geometry what parameters to use. For example, the strategy determines whether the bulk of the part or the perimeter is exposed first and how the rest of the sequence looks like, e.g., bulk followed by two perimeter exposures. The strategy also defines the laser scanning pattern during the exposure of the bulk, e.g., chess-pattern, stripe-pattern, unidirectional, etc. The parameters are the set values of the various components within a PBF-LB system, such as the laser power, the laser scan speed, the hatch distance, and the layer thickness.

Significant research efforts have been made to improve the quality of printed components in terms of the residual porosity, surface roughness, printed accuracy and the residual stress state [12]–[18]. Among the most significant process parameters that define part quality is the laser power, scanning speed, hatch distance and the layer thickness. A schematic detailing these is

given below in Figure 5. These can additionally be formulated into an equation that provides the volumetric energy density (VED) metric, expressed as follows:

$$VED = \frac{P}{V\,H\,L} \tag{1}$$

where P is the laser power (in W), V the laser scanning speed (in mm/s), H the hatch distance (in mm) and L the layer thickness (in mm). This metric provides a crude indication of the parameter-space, typically where sufficient part quality can be achieved. However, it does not include the laser spot-size or the laser intensity, nor any material specific properties. More refined heat-flow models, including the mentioned factors, were developed by Thomas et al. [19] and were based on the early work by Ion et al. [20].
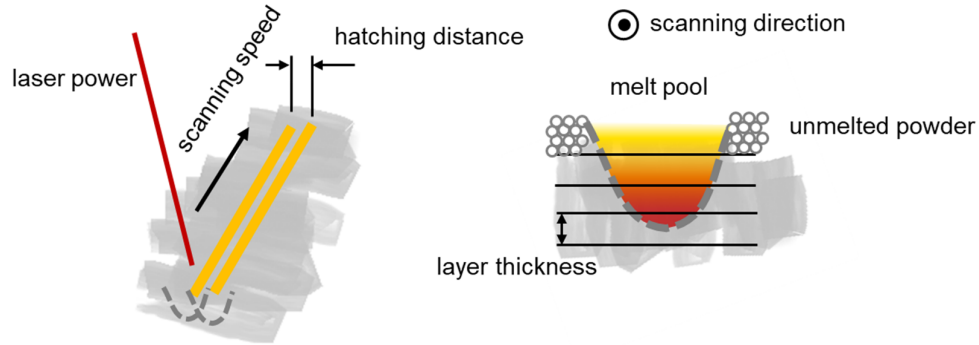

Figure 5. A schematic of parameters defined in the VED.

Apart from part quality, there has been major push to increase the productivity of the PBF-LB process as it is the main cost-driver of additively produced parts [21]. Many strategies include costly hardware modifications, including high-powered lasers and multiple laser sources [21]–[23], yet productivity boosts by process optimization is also a viable strategy. The productivity can be defined as the product of three parameters: the scanning speed, the hatch distance and the layer thickness. While the scan speed can be adjusted to run at its maximum capacity, 7000 mm/s, it is avoided as the available laser power will be insufficient to produce stable melt pools. This is also the case for the hatch distance. Hence, there are limitation to productivity gains using the two first mentioned parameters. Gains in the productivity using layer thickness optimization have been reported to be possible up to 4 times [24]. Further increases in the layer thickness was shown by Schwerz et al. [25] to generate excessive spatter that would incorporate into the built components hence leading to lack-of-fusion defects. Recent work by Pauzon et al. [26] has shown that by tuning the composition of the protective gas by additions of helium, it is possible to reduce the number of incandescent spatter particles during the printing process. Thus, possibly facilitating further layer thickness optimizations.

2.2.2 Influence of the powder properties

The PBF systems rely heavily on powder rheology to ensure that the powder can spread into thin, dense, and homogenous layers. Some systems, like the SLM Solutions machines, also require good powder flowability to ensure sufficient flow from the powder dispenser into the powder re-coater. Both terms, spreadability and flowability, describe the rheological properties under unique conditions – spreadability acts under the influence of external forces while

flowability acts due to gravity. Spreadability can be considered a form of flowability, but for the sake of clarity these terms will be kept separate.

Powder rheology depends on many powder characteristics and external conditions, including the powder size, its distribution, morphology, and humidity. To provide a complete picture of the complexity and interdependencies of powder rheology and the factors affecting it, a schematic is provided below in Figure 6. It would be impractical or too time-consuming to measure all of the listed properties to define the rheological properties of metal powder. As a step to provide a metric of the flow properties, the metal powder handling industries adopted methods that have been standardized to characterize the flowability. One of these methods evaluates flowability by measuring the powder flow through a standardized funnel, the Hall-funnel, with a 60 ° wall-angle and a 2.5 mm orifice in the bottom. This flowability test was initially developed for powder metallurgy (PM) to predict the flow of metal powder through bins, hoppers, feeders, and chutes [27], trying to mimic these flow-patterns. It is worth mentioning that all flowability measurements are only valid for the specific testing procedure and equipment. This means, powder that flows freely through the Hall-funnel (such powder is typically called free-flowing) cannot be guaranteed to be universally free-flowing.
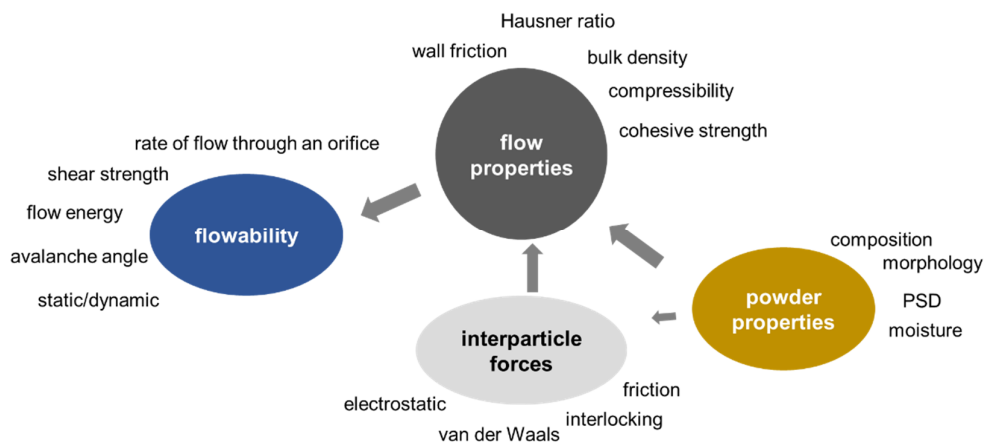
Figure 6. A schematic providing an overview of the factors that influence powder rheology. Re-drawn from [28].

The PBF-community has widely adopted the PM flowability testing for powder characterization. There are many reasons for this adaptation, the method is standardized according to ISO 4490 [29], the required equipment is readily available and at accessible cost, and the method has good repeatability and reproducibility with low demands on operator skill. Additionally, the funnel methods are the recommended methods to evaluate powder flowability within the ISO/ASTM 52907 standard, which describes powder characterization methods for AM [30]. Despite this, the Hall-flowability has also received notable criticism within the academia [31]–[37] for its application to characterize powder for PBF techniques.

One of the main critiques is that it measures the propensity for powder to free-flow through a funnel, rather than being spread, which is the major mechanism of powder transport in PBF. Even the ISO/ASTM 52907 standard notes that none of the described flowability tests "necessarily correlate to spreadability". Another point of criticism is that the Hall-funnel has

rather limited capability of measuring flowability when the particle size distribution (PSD) shifts to smaller sizes, as commonly found in PBF-LB powder. This shift increases cohesive forces between particles, potentially causing the powder to not flow through a Hall-funnel. As a powder producer, it can lead to rejection of powder batches as the Hall-funnel is often used as a quality assurance tool; even though that no clear link between Hall-flowability and spreadability has been established. Powder that does not flow through the Hall-funnel is, however, often spreadable and printable.

The critique has led to the implementation of new powder characterization equipment for PBF. One of these is a powder rheometer, Freeman FT4, developed by Freeman Technology. It can measure various static, dynamic, and shear properties with a claimed high precision. Another is the group of rotating drum analyzers, such as the Revolution Powder Analyzer (RPA) by Mercury Scientific or the GranuDrum by Granutools. As the name suggests, the equipment analyzes the avalanche angle of powder as the drum is rotated. Both have been shown to extend the measuring range of the Hall-funnel [35], [38], [39], capable of measuring powder with no Hall-flowability. Despite this, it is still not clear how the RPA and FT4 flowability measurements correlate to spreadability, and in extension how suitable a powder batch will be for LBF-LB. This can be due to several factors, both provide numerous metrics that can be difficult to link to spreadability, with a compounding factor that there are no available standards for these tools. This has led to that many authors choose to present different metrics in their publications, something that complicates direct correlation between different studies.

As mentioned, there are multiple studies that have used the RPA or the FT4 for flowability characterizations of PBF-LB powder, showing that both are capable to differentiate between virgin and re-used powder, powder batches, etc. [40]–[47]. Regardless, there are relatively few studies that connect the flowability properties to the printing performance, or the ability of a printed part to reach full density. Riener et al. [48] studied the powder properties of different AlSi10Mg powder grades using several techniques, including an RPA and a self-developed re-coating system for layer density analysis. It was found that the powder with lowest avalanche angle (AA, RPA measurement) also gave rise to the greatest layer density, and during printing had the lowest residual porosity. No other RPA metrics apart from the AA was given. Seyda, Herzog and Emmelmann [49] performed a similar study, with three Ti-6Al-4V powder grades where flowability measurements using both the RPA and the FT4 were done. Contrary to the study of Reiner, Seyda found that powder with the highest measurable flowability did not produce components with highest density. Rather, it was the powder with lower flowability that attained highest density. This was also reported by Strondl et al. [34] in a recyclability study where the recycled powder had better flowability yet produced more porous parts. Seyda, Herzog and Emmelman [49] also showed that generally the results of the RPA and FT4 correlated well, specifically the AA with the specific energy of the FT4.

The paragraph above is not intended as an exhaustive literature review, rather it is intended to capture the complexity of the flowability measurements for PBF-LB. In some literature, powder with best flowability coincides with the densest parts, sometimes it does not [47], [49], [50]. Some recent phenomenological studies can help provide some further needed context. The effective powder layer before laser exposure is often considered to be solely related to the density of the powder layer (typically above the apparent density), reaching steady state after a few layers. However, Wischeropp et al. [51] showed that it can be up 5 times the actual layer height. These findings were also confirmed by Liu et al. [52] who used correlative in-situ

thermographic imaging to predict the effective powder layer thickness, which was found to be 4 times the nominal layer thickness. The causes behind this are spatter generation, powder denudation during exposure, and vaporization. Another topic of interest is the actual spreadability of powder, typically trials are conducted on machined surfaces, or on artificially altered surfaces as opposed to the actual "as-printed" surfaces. Here, Phua et al. [53] showed through simulations that despite lower flowability finer powder spreads more homogenously on as-printed surfaces – where the smallest particles effectively fill the valleys of the surface roughness profile.

In consideration of the contents within this section, the importance of defining a methodology that provides a metric for how suitable a powder is for PBF systems becomes clear. Spreadability alone can be misleading as it only entails the spreading of powder. Even powder with low flowability, such as water atomized powder grades, are spreadable and printable to high densities [54]. What limits their performance is the low powder bed density [55]. In some sense, we need to re-define our concept of flowability within the context of PBF – fastest through the Hall-funnel is not always the best.

2.2.3   Laser–powder interactions

This section aims to provide some insight in to how the laser source interacts with powder to form a melt track, how this melt-track is maintained and some of the phenomena occurring during the exposure. Additionally, some basic laser welding concepts are introduced.

A laser beam is a focused high-intensity source of photons, whose energy is transferred onto the surface of the work piece. Contrary to a flat surface, a bed of powder has the possibility to reflect the beam multiple times before the beam is scattered. Hence the laser absorptivity of powder is higher relative to a flat surface, with reported values of between 0.6 and 0.7 for stainless-steel powder [56] compared to 0.4 for a bulk stainless-steel surface [57] using a laser with a wavelength of 1053 nm. The heat-transfer in PBF-LB is very rapid, with each metal powder particle being exposed to the laser beam roughly 0.1 ms (under typical scanning speeds of 1000 mm s^{-1}). This causes a concentration of the thermal energy at the skin of the metal powder particle, which almost instantaneously (around 10 µs for a 50 µm particle) transfers to the bulk of the particle [58]. During the simultaneous melting of several particles, the melt pool is formed.

In laser welding the parameters are often tuned to operate under the "key-hole" mode, where the melt-pool assumes the appearance of a key when it hangs down from a key-chain – which ensures deep penetration of the weldment. Another mode with lower penetration is the conduction mode, where the key-hole is suppressed. The key-hole forms when high laser powers are used, causing the melt to locally boil and vaporize – with the vapors potentially forming a plasma. The vaporization gives rise to a vapor pressure, acting in a direction normal to the surface. This causes the melt pool to "dig" deeper, as the molten material is pushed from the point of irradiation [59]–[61]. Another mechanism that contributes to the formation of a key-hole is the Marangoni flow.

The Marangoni flow is a hydrodynamic flow caused by changes in the melt viscosity as a function of the temperature [62]. As the melt cools, the viscosity increases relative to the melt that is at a higher temperature – under the assumption that the viscosity decreases as the temperature increases. This creates a flow of the melt that is typically directed from the hotter

sections to the colder sections, seen in Figure 7. In the presence of high thermal gradients, the Marangoni flows generate a strong mixing effect within the melt pool, and can be strong enough to eject molten material from the melt pool [63]. The latter constitutes a part of spatter – a PBF-LB by-product consisting of particles that land on the powder bed, including the surfaces of freshly laser exposed parts.
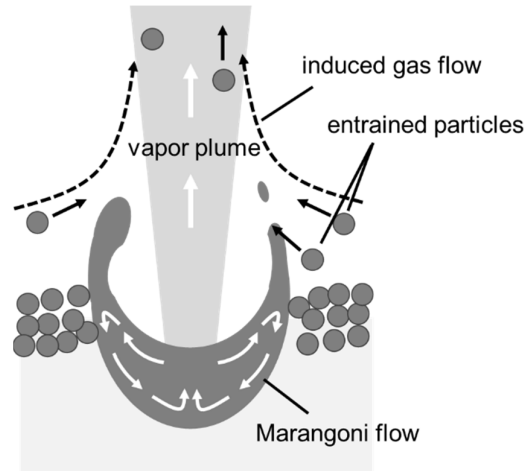
Figure 7. Schematic of the melt pool, its Marangoni flow and the associated gas flows.

Under typical PBF-LB processing conditions the laser operates in the conduction mode [64]. However, due to the high intensity of the laser there is considerable vapor plume formation even in this mode, which can be clearly imaged by shadowgraphs. The plume generates a strong vapor flow, as seen in Figure 7, causing a pressure drop around the melt. Due to the pressure drop there is a secondary inward flow of cold processing gas [56], [65]. The flow is strong enough to carry metal particles (entrained particles) – causing both denudation of powder adjacent to the melt track [65]–[67] and spatter generation as metal particles are caught in the flow of the vapor plume. Pauzon et al. [68] showed that some of the spatter can, during its flight, cross into the laser path and incandesce, potentially fusing spatter agglomerates into larger particles. Such large particles cannot be effectively carried away by the shielding gas and end up on the powder bed. If exposed by the laser, these particles can result in disruptions of the melt pool – resulting in the formation of residual porosity as the energy is insufficient to properly melt these [26], [69], [70].

In-situ studies that has specifically looked at laser, powder, and melt-pool formation have been more limited. This is mostly due to the experimental complexity of such work. However, Leung et al. [71] presented in-situ X-ray imaging of laser-powder interactions. It could be seen that powder that was adjacent to a freshly formed melt-track was ejected. However, it should be mentioned Leung et al. used relatively slow scanning speeds, atypical of conventional processing parameters. Recent work of Pauzon et al. [68] also presented in-situ radiography results with parameters that better resemble those that are typical in PBF-LB. Similar observations were done, powder particles adjacent to a melt track are ejected. This ejection is caused by the rapid heating of the gas in the inter-particle voids, which rapidly expands and powder particles are ejected. This suggests that the density of the powder bed is a significant factor for PBF-LB performance, as this means that less gas gets superheated during the melt-pool formation.

3. Powder manufacturing

Metal powder is commonly produced through a process called atomization, where liquid metal is transformed into small particles by means of a pressurized matter, e.g., gas, water or plasma. This process can be likened to water sprinklers, or simple spray nozzles in cleaning supplies, albeit very simplified, that turn a liquid into a fine mist. Apart from atomization there are other ways to manufacture powdered goods, such as milling, crushing, through chemical processes, and spray drying [72]. However, these methods are rarely used in powder manufacturing for AM.

Powder for AM is typically produced using advanced technologies to be able to meet the stringent specifications that are often put on AM powder. Such specifications often include limits on the residual oxygen content, impurity contents including sulfur and phosphor, and requirements on optimal flowability and packing efficiencies. Such pre-conditions originated from the early days of AM, when it catered to small-scale niche applications such as dental implants and medical equipment [73]. Hence, requiring vacuum technology and high-purity gases that drove the powder cost up. As AM evolved, more materials were included in the materials portfolios of machine suppliers. Despite having materials that conventionally do not require vacuum processing, the majority were produced using vacuum technology.

As AM continues to grow and advance as a technology, it is only natural that the evaluation of suitable powder manufacturing routes continues with it. For the technology to be able to trickle down to more cost-sensitive applications, there needs to be concurrent development and feasibility studies of lower-cost powder grades for the various AM technologies.

The following chapter aims to introduce some of the conventional AM powder production routes together with some powder manufacturing techniques that have not been common for AM. However, the focus will on gas atomization (GA) as it constitutes the bulk of the powder production for AM. A short summary of the methods is given below in Table 1.

Table 1. A short summary and comparative metrics of powder produced with techniques capable of producing powder for AM.

Powder production route	PSD, µm	d_{50}, µm	Melt flow rate, kg min^{-1}
Electrode induction-melt gas atomization	10-500	90-140	<2 [74]
Gas atomization, free-fall	5-300	100	6-80 [72]
Gas atomization, close-coupled	5-200	50	2-40 [72]
Plasma atomization	0-150	40	<1 [75]–[77]
Water atomization	0-500	70	1-500 [72]

3.1 Gas atomization

Gas atomization, specifically vacuum inert gas atomization (VIGA) is the atomizing technology that produces most of the powder for AM. Powder produced with GA is spherical, with visible dendrites on the surface, as seen in Figure 8. The powder has good flowability and packing efficiency, reaching up to 60% relative to its full theoretical density. Additionally, as seen in Table 1, the GA powder also offers comparably high melt flow rates, which accelerates the production capability. The technology is suitable for different material groups including Fe-based alloys, Ni-based alloys, Co-based alloys, and Cu-based alloys. It is, however, less suitable to produce Ti and Al-based alloys as these tend to dissolve the furnace lining – causing

premature lining failure and excessive ingress of lining material into the atomized powder. Despite this, there is ongoing research on refractory ceramics that are capable of withstanding these materials in their molten states [78]. A schematic of the GA process is provided in Figure 9.
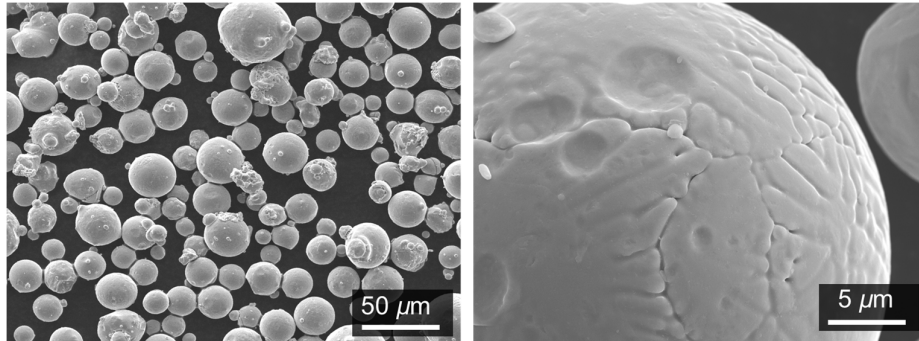
Figure 8. 316L VIGA powder at low and high magnifications.

3.1.1 Melting

The GA process starts with melting of the powder pre-cursors. Here, the process can be split into two segments: one where melting occurs under vacuum and one where it does not. The furnaces are commonly heated using induction coils, which also stir the melt once all of it has liquified. Relative to VIGA, conventional gas atomization (CGA) operates under full exposure to air. Naturally, this comes with both benefits and drawbacks.

Figure 9. A schematic of the gas atomization process, with a detailed view of close-coupled and free-fall nozzles.

The benefits are all due to that the melt is easily accessible for manipulation. Conventional melt processing heavily depends on this to both clean the melt, and to ensure that it is within the compositional specifications. As liquid metal is highly reactive, it naturally forms a buoyant

16

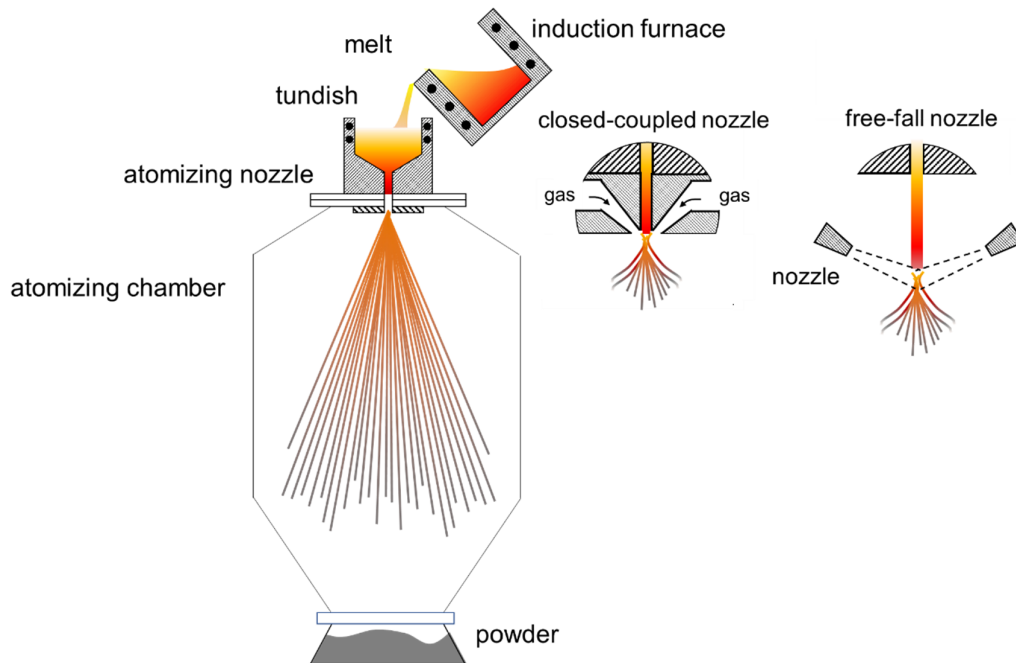cap of liquid oxide – the slag layer. Often, synthetic slag is added to the melt to adjust the slag pH and viscosity [79]. This slag acts as a diffusion barrier for oxygen, effectively protecting the melt from further oxidation. The melt can be purified from sulfur and phosphor by additions of quicklime and magnesite, both that react with said elements forming compounds that float up into the slag. The slag can be utilized even further, to de-carburize the melt and to recover oxidized metal from the slag by injecting carbon into the surface of the melt. Another benefit is that the composition can be tested and adjusted more easily during air-melting. The main drawback is the lacking ability to process highly reactive elements, e.g., Ti and Al, in high amounts. As these elements have high affinity to oxygen, they will oxidize and migrate to the slag layer. Due to the high thermodynamic stability of their oxides, these elements cannot be easily recovered by carbon injection.

A process that can accommodate high amounts of reactive elements is the VIGA process. This is accommodated by the bulk removal of oxygen through vacuum technology. As the whole system is pumped down to a 10^{-3} mbar vacuum [80] using extensive pumping infrastructure, the charging (the raw materials that will melt and form the final alloy) has to be carefully calculated and prepared prior to furnace evacuation. Typically, smaller facilities (common in powder manufacturing) do not have capabilities to adjust the alloying once melting begins. When processing Ni-based alloys the melting begins with the non-reactive elements, where a small amount of carbon is added in a procedure called the "carbon boil" [81]. The purpose is to remove most of the residual oxygen by forming CO and CO_2 gases hence the name boil – only afterwards are the reactive elements added. The remaining residual oxygen is removed through the melt/vacuum interface, which is enhanced by the continuous stirring of the melt by induction coils. It is still, however, a slow process. Further melt refining, as possible in the CGA process is limited. Thus, there are high requirements on the raw-materials hence scrap based raw materials are seldomly used.

To prepare the melt for atomization, it is super-heated above its melting temperature. This is done to reduce the viscosity further and to compensate for heat-losses during the next steps, which will be described in the next section.

3.1.2 Atomization

Compared to the melting process, the step of atomizing the melt is similar between CGA and VIGA. After super-heating the melt it is transferred to a separate intermediary crucible called the tundish. The role of the tundish is to neutralize the currents previously induced in the furnace, so that the atomizing nozzle receives a steady flow of liquid metal. The atomizing nozzle is situated directly below the tundish and the liquid metal flows through an orifice at the bottom of the tundish. The orifice diameter is an important parameter in powder atomization, and it is optimized for a specific mean particle size and PSD. Increasing it causes the mean particle size to increase and the PSD to widen, and vice versa. If the orifice diameter is decreased too much, a phenomenon called freezing can occur. Freezing take place when there is insufficient flow through the orifice – causing accumulation of solidified metal at the orifice wall. Eventually the orifice gets blocked by solidified metal and the atomization process is interrupted.

The atomizing nozzles are generally separated into two types: close-coupled nozzles and free-fall nozzles (see Figure 9). Both utilize a highly pressurized gas, up to 20 MPa yet 3 MPa is more common, to break-up the melt stream into fine droplets. The atomizing pressure is another

17

PSD defining parameter, which can be tailored to better fit the target mean particle size. The gas is either argon or nitrogen, depending on the reactivity of the melt. Nitrogen offers some thermal benefits to argon and is soluble in the matrix of few alloying systems. Close-coupled nozzles are generally used for finer powder production, as the yield of sub 50 μm particles increases as compared to a free-fall nozzle, which has been reported to be around 15% [82] for a 25-63 μm sieve cut. The close-coupled nozzle sits directly underneath the tundish, hence its name. This ensures that most of the energy in the atomizing gas goes to melt stream disintegration. Further optimization of the nozzle design can provide an even better control of the PSD, as shown by Ünal [83].

There are a few drawbacks of the close-coupled nozzle, including erosion of the nozzle, increased tendencies for freezing, and satellite formation. Due to the proximity of the nozzle to the melt-stream, there are strong induced thermal gradients within the nozzle – eroding it thus making the nozzle a consumable. The freezing and satellite formation originate from the strong gas turbulence that is induced by the close-coupled nozzle. The gas exits the close-coupled nozzle as a cone, impinging the melt stream at its apex. The perimeter of the cone has a very high velocity causing the inside of the cone to drop in pressure. This effect pulls both particles and droplets back into the tundish orifice, possibly causing build-up at either the orifice or even the nozzle itself resulting in a clogging or freezing [84]. The severity of this issue can be remedied by nozzle design, where some of the atomizing gas is introduced into the cone hence reducing the vacuum that is otherwise produced there. Finally, the last detrimental effect of the turbulence is satellite formation, namely when smaller particles weld themselves onto larger droplets that have not fully formed a solid outer skin [82]. An example of excessive satellite formation can be viewed below in Figure 10. The phenomenon is very detrimental to the powder flowability – often causing rejection of the powder batch.
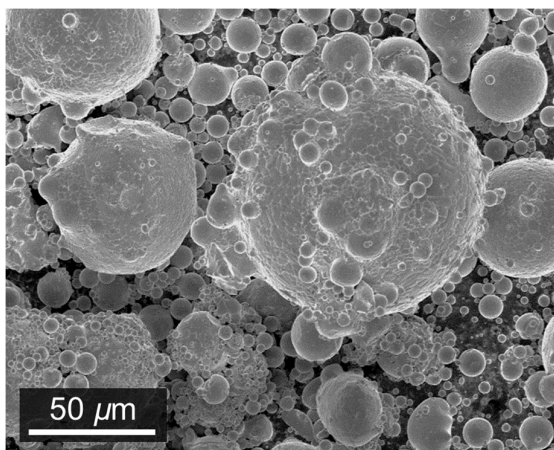
Figure 10. Powder atomized with a close-coupled nozzle with excessive satellite formation.

The free-fall nozzle sits at a distance from the tundish orifice – allowing the melt to free-fall prior hitting the gas stream. This greatly reduces the amount of turbulence within the atomizing chamber – in extension also reducing the tendency for satellite formation and provides a more reliable process. As the gas jets are located at a greater distance from the melt stream, they lose more energy, relative to a close-coupled nozzle, before impacting the liquid melt stream. This significantly impacts the ability for the gas to disintegrate the stream into fine droplets – resulting in an increase of the mean particle size.

Finally, the topic of internal gas porosity within powder particles was extensively researched by Rabin et al. [85]. It was found that internal porosity is mainly caused by melt ligaments collapsing on themselves – forming a bubble. However, the potential effect of saturated inert gas precipitating out in the form of pores from the superheated melt cannot be fully excluded. Much of the gas porosity was found in particles above 75 μm in size.

3.2 Electrode induction-melt gas atomization

Electrode induction-melt gas atomization (EIGA) is in many aspects very similar to GA, with the key difference that it is a "crucible-free" atomizing process. Hence, the liquid metal is never in contact with any furnace refractory materials. EIGA is therefore used to atomize materials that either have very high melting temperatures or are very aggressive to the refractory linings. Examples of such metals are Ti-alloys, Al-alloys and the refractory metals Zr, Nb, and Ta. To circumvent the issue of furnace melting, the raw material is supplied in the form of pre-alloyed rod-shaped electrodes (up 150 mm in diameter). To produce a stream of liquid metal the rod tip is surrounded by induction coils that melt it at a rate that provides suitable flow rates to the atomizing nozzle [86], [87].

As the method is crucible free, only the free-fall nozzle can be used during atomization. Hence, the resulting PSD and mean particle size is similar to the GA process with a free-fall nozzle. It is, however, possible to reduce to melt-stream rate even further as there is no tundish orifice that can freeze – making it possible to shift the PSD to even smaller sizes.

3.3 Plasma atomization

Plasma atomization is another crucible-free powder production method, which is primarily aimed at materials that are difficult to melt and atomize otherwise. Contrary to the EIGA process, the raw material is supplied in the form of either a single or dual wires with a diameter between 1 and 5 mm. The wire, or wires are fed into a plasma torch, or several torches that simultaneously melt and atomize the powder. The plasma torch (non-transferrable) is generated by the ionization of an inert gas, such as argon, by an electric discharge, which heats it to temperatures of ~11000 K [76]. Only a fraction of the gas is ionized, with the remaining gas heated to temperatures between 2000 and 10000 K by the generated plasma. This mixture of heated and ionized gas is accelerated through supersonic nozzles and reaches very high velocities thus simultaneously melting and atomizing the wire.

The resulting powder has nearly perfect spherical shape, minimal internal porosity, and only minor tendencies to form satellites. The resulting PSD is comparatively narrow with a mean particle size of 40 μm, thus making it ideal for PBF processes [75], [76]. Plasma atomized powder, however, comes at a high cost. This is mostly due to the slow throughput, energy consumption [75], and cost of the pre-alloyed wire [86].

3.4 Water atomization

Water atomization (WA) is not frequently used for producing powder for the AM processes, despite that its feasibility in the PBF-LB process has been shown [54]. Contrary to the methods described above it does not produce very oxygen lean, nor well-flowing powder and cannot process large quantities of reactive elements. Yet, the production technique lends itself well to produce large quantities of powder, significantly exceeding CGA, VIGA, EIGA and PA – pushing the powder cost down significantly. Another advantage is the opportunity to produce

extremely fine powder with narrow PSD's by using high water pressures. This is due to the properties of water, such as its high density and high heat capacity, as compared to gases. Hence, this allocates large amounts of energy for melt disintegration. With the capacity of delivering plenty of kinetic energy to the melt stream, also comes the capacity of rapidly cooling the fine droplets – which effectively freezes their irregular shape, with limited time for the surface tension to alter the shape. A representative image of water atomized powder is shown below in Figure 11.
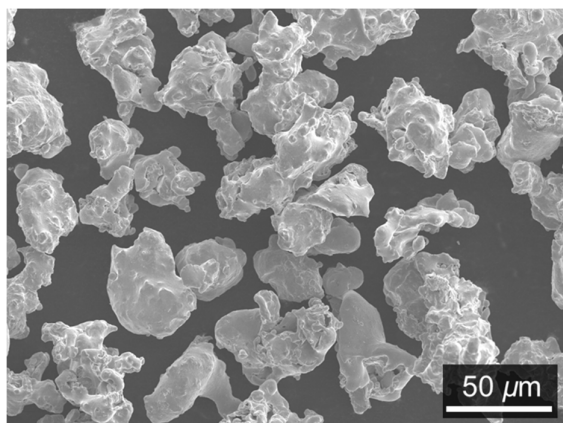
Figure 11. Micrograph of water atomized 316L powder.

When atomizing, there are several nozzle designs to choose from. Among the common ones are the annular cone and the V-jet nozzle [84], which are displayed below in Figure 12. In powder production for the PM route of press and sinter, pressures of 10–15 MPa are used – rendering a mean particle size of 70 μm. Higher pressures, up to 150 MPa, in combination with V-jet nozzles are used to produce fine WA powder, where it is possible to reach a mean particle size below 10 μm [88]. A reason for the ability of the V-jet nozzle to produce such fine powder is that owing to the high water-jet velocities a low-pressure zone is formed above the point where the jets coincide. This causes the melt-stream to pre-atomize before it hits the jets [88]. It is possible to further tune the nozzle design, (distances, jet angles, etc.) to reach a PSD that is more suitable for the intended process.
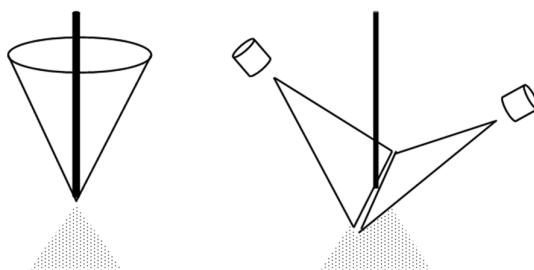
Figure 12. Atomizing nozzles used in WA, to the left an annular cone nozzle, to the right a V-jet nozzle.

Powder produced using WA will inadvertently have some oxidation, there are however means of mitigating it. Many of these strategies involve the use of an inert gas. A common approach is filling the atomizing chamber with it, which serves two purposes. One is to reduce oxidation of the particles as they are cooled. Another, perhaps more crucial, is to avoid hydrogen explosions when the water dissociates during atomization [89]. A novel approach by Takeda et al. [90] is to introduce the inert gas within the atomizing nozzle itself, resulting in some

reduction in oxidation but more importantly serves to disintegrate the stream prior to the water jets. This process is called hybrid atomization and is used to produce very fine water atomized powder.

4. Oxidation of powder

4.1 Thermodynamic considerations

The aim of this chapter is to provide a thermodynamic introduction to oxidation of metals, the driving forces for oxide formation and their stability relative to their metal states and other oxides.

A chemical reaction takes place due to its driving force to reduce its total energy state. Without it, chemical reactions would spontaneously not occur. This driving force is defined according to the change of the Gibbs free energy ΔG. This change is from the state that the substances (reactants) are in prior to the reaction to after the reaction (products). A chemical reaction will only occur if the ΔG is negative, hence the products will always have a lower energy state relative to the reactants. This is also why most metals are found in their oxidized state, as it is more energetically favorable. The change in the standard Gibbs free energy (formation of 1 mole of the substance from its component elements, in their standard state, the most stable form of the element at 25 °C and 100 kPa) is defined according to the following equation:

$$\Delta G^0 = \Delta H^0 - T\Delta S^0 \tag{2}$$

Where H is the enthalpy of the system, S is the entropy, both in Joule, and T is the temperature in Kelvin. The Gibbs free energy can be formulated to include the equilibrium constant of a reaction, as follows:

$$\Delta G = \Delta G^0 + R\,T \ln K \tag{3}$$

where R is the gas constant and K is the equilibrium constant. The equilibrium constant is used to determine the quotient between the reactants and the products at chemical equilibrium, e.g., the ratio between oxide and metal as well as the involved gas species. Once equilibrium has been reached, $\Delta G = 0$, the standard Gibbs free energy is:

$$\Delta G^0 = -R\,T \ln K \tag{4}$$

The equilibrium constant K relates the activities of all species within the reaction, and is defined accordingly (for a general reaction):

$$bB + cC \rightleftharpoons dD + eE \tag{5}$$

$$K = \frac{a_D^d\,a_E^e}{a_B^b a_C^c} \tag{6}$$

where the lower-case letters represent the mole concentration of each sustenance, and a is the activity of that substance. Generally, if K is larger than 1 then the quantity of products is favored, and if K is below 1 then the reactants are favored. For metals reacting with oxygen, the general equation is:

$$\frac{2x}{y}M + O_2 \rightleftharpoons \frac{2}{y}M_xO_y \tag{7}$$

To simplify, the metal and oxide activity are approximated to be unity and therefore the K constant can be written accordingly, where $p(O_2)$ is the partial pressure of oxygen:

$$\Delta G^0 = -R\,T \ln p(O_2) \tag{8}$$

23

Equation 8 is the basis for Ellingham diagrams, which plot standard Gibbs free energy changes as a function of the temperature for various oxides. An Ellingham diagram with selected oxides is shown in Figure 13. Generally, the stability of oxides is decreased as the temperature increases, visualized by the positive slope of the curves in the diagram. In more conventional Ellingham diagrams, it is also possible to obtain the equilibrium partial pressure of O_2 throughout the temperature scale.
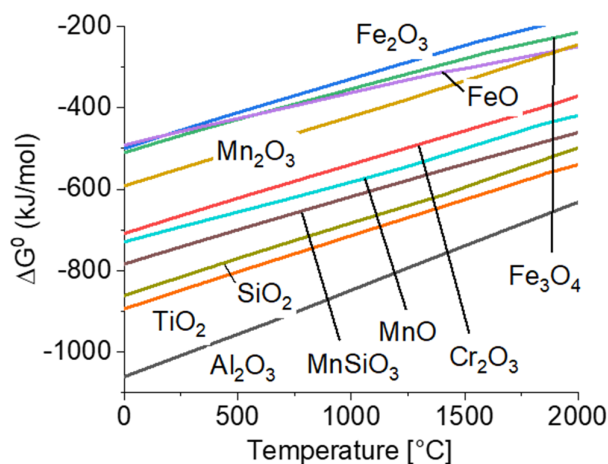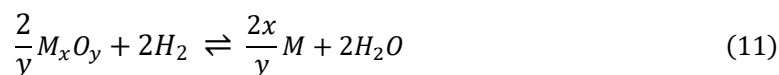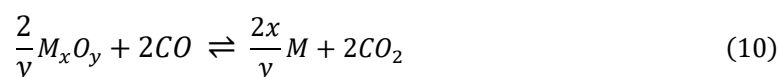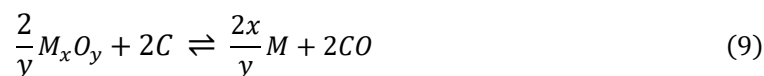

Figure 13. Ellingham diagram for selected oxides, data from HSC Chemistry 9.

Additionally, Ellingham diagrams typically include other partial pressures that are relevant for metal oxidation/reduction. These include the carbothermic reactions, both the direct (where C is the reactant, eq. 9) and the indirect (where CO is the reactant, eq. 10), and the hydrogen reaction (eq. 11). All are stipulated below:

$$\frac{2}{y} M_x O_y + 2C \rightleftharpoons \frac{2x}{y} M + 2CO \tag{9}$$

$$\frac{2}{y} M_x O_y + 2CO \rightleftharpoons \frac{2x}{y} M + 2CO_2 \tag{10}$$

$$\frac{2}{y} M_x O_y + 2H_2 \rightleftharpoons \frac{2x}{y} M + 2H_2O \tag{11}$$

4.2 Surface oxide state of the powder

The surface oxide state of powder has been a topic of researchers since pre-allowed powder grades started being atomized and utilized in the production of components. Fabrication of components using powder was primarily through the PM routes of press and sinter, and hot isostatic pressing. As pre-alloyed powder grades frequently contained elements sensitive to oxidation, these would preferentially oxidize during atomization on the powder surfaces either as particulates or continuous oxide films. These surfaces would be entrapped during the compaction and subsequent sintering operations. The trapped oxides, when mechanically loaded, would either crack or act as decohesion sites – leading to serious degradation of the mechanical properties [91]–[94]. Hence, there was an urgency to research and understand the formation of oxides and to develop strategies on how these oxides could be reduced. Either during atomization by improving atomization practices or during the sintering cycle by

introducing reducing agents or by employing high temperature sintering. This section serves as introduction to surface oxidation of powder, how atomizing media affects it, and how to characterize the surface oxidation.

Surface sensitive characterization techniques such as X-ray photoelectron spectroscopy and Auger electron spectroscopy were employed in the pioneering work in the early 1980's by Olefjord and Nyborg [91] to characterize metal powder. The challenge of these techniques is the angular dependence of electrons that are emitted from a non-planar surface. Olefjord, Nyborg and Nylund developed geometrical relationships that enabled an analysis of spherical particles – proving a methodology to estimate the surface oxide thickness [95]. Of the earlier efforts, investigations of nitrogen atomized stainless ferritic chromium steel powder revealed that the powder surface is predominantly covered by oxide particulates, described as protrusions on the powder surface. Both, the speciation, and the coverage of these particulates relative to the total area was analyzed. The particulates were rich in Cr, Mn and Si – elements with highest driving forces for oxide formation. Additionally, Olefjord and Nyborg reported that a Fe_2O_3 layer, less than 5-6 nm thick, was present between the particulate islands. Later, it was theorized that the particulate compounds form during the atomization process, whereas the iron oxide layer forms during powder cooling and handling [91]. This research set the stage to what kind of analysis was possible on powder using advanced surface characterization techniques and outlined the general model by how powder oxidizes during the atomization process.

Research on different factors affecting surface oxidation of metal powder continued. Including how the particle size influences the formation of surface oxides during atomization. Norell and Nyborg [96], [97] found that during atomization of a martensitic 12Cr stainless steel, particles with an average particle size of 40 μm and above had an overall average oxide thickness of 6 nm, rich in Fe, Cr and Mn. Particles smaller than 40 μm had however, a thinner oxide layer yet were enriched to a higher extent in Cr and Mn relative to the larger particles. Furthermore, Nyborg et al. [97] investigated effects of varying quantities of residual oxygen within the inert atomizing atmosphere when preparing powder of the same composition, by means of rotating electrode process atomization, as in the earlier mentioned studies. The effect was similar to the size effect, as the oxygen content was gradually reduced elements with the highest oxygen affinity would preferentially oxidize. Using high purity argon gas, it was found that Si had significantly oxidized while the remainder of elements had weak or insignificant oxide peaks within the spectra. Thus, as the available oxygen is reduced there is a competitive growth between elements with the highest oxygen affinity (see Ellingham diagram in section 4.1), e.g., Mn, Ti and Si. Additional factors such as diffusion rates and element concentrations will also play a role. Elements with sluggish diffusion and low concentration might be easily exhausted at the top surface, where the primary oxidation is occurring.

The application of surface sensitive techniques was later extended to non-spherical powder, such as WA powder. Nyborg and Tunberg [98] showed that the average surface oxide thickness was comparable to GA powder when the particle size was below 50 μm for stainless 304L powder, which was connected to the high cooling rates involved in WA. Particles with rapid cooling rates had elements with high oxygen affinity preferentially oxidized at the surfaces, like the surfaces of GA powder sizes below 40 μm, or when atomized with high purity gas. The difference to the GA process is that the rate-limiting factor for oxidation is the high cooling rate, hence governing both oxide composition and its thickness. Tunberg and Nyborg [94] continued investigating WA 304L powder with additions of either Si, Al or C. In the case of Al

additions, the limitations of WA on processing reactive elements were clear. The atomized surfaces were predominantly covered by Al cations, in fractions ranging from 0.45 to 0.75, depending on the particle size. This led to a deterioration of the elongation to fracture in sintered components, reaching below 0.03%. Hence, despite the rapid cooling the oxygen availability in WA enables oxidation of elements with high driving forces.

4.3 Oxide characteristics and their impact on the properties of PBF-LB components

Conventional PM fabrication routes involving sintering enables the observer to track changes in the surface oxides, as either their residues or unreduced oxides will be visible along the prior particle borders. The phenomenon is most prevalent in hot isostatic pressing [99], [100], as the process provides limited opportunities for oxide reduction. In AM, especially PBF techniques, this opportunity is lost as the powder particles are melted, violently stirred and solidified all within a few milliseconds. Therefore, the oxide transfer between powder and component is more difficult to establish. Oxides are commonly present within PBF-LB components [3], [101], the question is whether they transfer from the powder or form due to oxidation of the melt pool. If established, it can help provide insights into the importance of the surface oxidation state of powder for PBF-LB processed components. There is, however, quite limited amount of research detailing both surface oxide state of powder and the oxides found in PBF-LB processed components.

Gruber et al. [102] showed that during PBF-EB processing of IN718 powder the Al-rich oxides that had been previously characterized on the powder surface were found to melt, partially agglomerate, and finally solidify into micrometer sized inclusions. This shows that despite the high temperatures of the melt-pool in PBF-EB, oxides remain and become dispersed within the melt-pool due to strong Marangoni flows rather than dissolving and re-precipitating. Gruber argues that most of this oxide agglomeration is due to powder re-use – causing re-distribution and growth of oxides on the surface, eventually leading to deterioration of the mechanical properties [102].

Raza and Fiegl [103], [104] connected extended powder re-use to both, deteriorating mechanical properties and increased porosity in PBF-LB processed AlSi10Mg. In an extensive powder characterization study, it was shown that as powder was re-used the oxide layer kept growing. After 30 months of re-use the average oxide layer had grown to ~38 nm, as compared to 4 nm when the powder was in its virgin state. It should be noted, that a significant contribution to the increasing oxide layer was from the growing amount of heavily oxidized spatter particles, amounting to nearly 3% after 30 months [103]. Hence, not all powder particles undergo this severe oxidation from powder re-use.

Schwerz and Raza [25] explored spatter particles and their influence on the build quality, when PBF-LB processing the alloy HX with high layer thicknesses (up to 150 µm). They reported that extensive spatter re-deposition caused large lack-of-fusion type defects, extensively deteriorating the integrity of built components. As the spatter particle lands on a solidifying melt-pool, it creates a secondary solidification front, resulting in incomplete bonding between the spatter particles and the remaining melt-pool. XPS analysis of the spatter particles showed that they are heavily oxidized, with an oxide layer of ~80 nm consisting of mainly Al, Ti and Cr based oxides.

5. Strengthening mechanisms of stainless steels

Stainless steels constitute a class of ferrous alloys that are resistant to oxidation, making them suitable for use in corrosive environments or for elevated temperature applications. The main element behind this property is chromium and generally all stainless steels have at least 11wt.% in their composition [105]. The addition of chromium causes a passivation of the surface by forming a continuous chromium-rich oxide film. The corrosion resistance can be tailored by adding larger quantities of chromium together with additions of nickel and molybdenum. However, these additions will also influence the phase stability of the stainless steel. Stainless steels are generally single-phased, except for the duplex grades. Hence, stainless steels are divided into sub-groups that are defined according to its main stable phase. The common stainless steel families are:

- Ferritic grades
- Martensitic and precipitation hardening grades
- Austenitic grades
- Duplex grades

The different grades will have different properties in terms of corrosion resistance, strength, and weldability. For example, the austenitic grades typically have very high resistance of corrosion and are therefore suitable for the harshest environments. Yet their strength or hardness compared to the duplex or martensitic grades is relatively low [105]. Therefore, in applications where there are high requirements on strength, abrasion and wear they will be less suitable. For stainless steels, achieving high strength is a balancing act with the corrosion resistance.

The strength of a material can be defined as its ability to resist the motion of dislocations when an external stress is applied. The resistance is created through internal stress fields, obstacles and interfaces, and other dislocations [106], these are termed strengthening mechanisms. There are numerous ways of achieving this in stainless steels, some that are less detrimental to the corrosion resistance than others. These can be simplified into two main strategies: changing the composition of the alloy and by various processing routes (e.g., cold rolling or heat treatment). The thesis has focused on the austenitic and the martensitic precipitation hardening grades, therefore the focus will be on the strengthening mechanisms that are involved in these grades.

5.1 Solid solution strengthening

Solid solution strengthening is one of the fundamental methods of increasing the strength of a pure metal. The principle of solid solution strengthening is the introduction of one or more elements to the base metal, which are incorporated into the crystalline lattice of the metal. Depending on the size of the solute atoms, the crystalline lattice of the metal will expand/contract. This expansion/contraction forms stress fields that provide hindrance to dislocation movement, this effect is called the elastic misfit interaction. The magnitude of the stress field will be dependent on the size of the solute atom and how it is situated in the lattice.

There are two ways that a solute can fit within the lattice, either interstitially or substitutionally. These two modes are presented below in Figure 14. Interstitial solutes (imaged black in the figure) are often smaller atoms, such as carbon and nitrogen, that fit in-between the solvent atoms (imaged grey in the figure). Substitutional solutes (imaged striped in the figure) are situated in lattice points where the solvent atoms would have been and are often closer in size

to the parent lattice atoms that they are substituting. The solubility of the substitutional atoms will be governed by both the atom size misfit and the similarity of their native crystal structure [107]. If the solubility is exceeded, both in terms of interstitial and substitutional solutes, a new phase can precipitate, decreasing the number of solute atoms within the lattice. Hence, there is a limit to how much can be accomplished through solid solution strengthening.
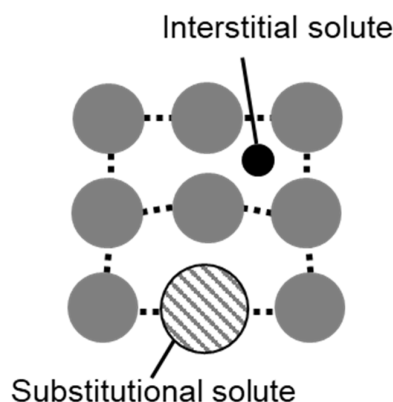

Figure 14. Crystal lattice and positions of interstitial and substitutional solutes.

In the presence of an edge dislocation, there will be an additional half-plane above the slip plane. This will give rise to a compressive stress above the slip plane and a tensile stress below it. As solutes create stress fields around them due to the lattice dilation, this stress field could be minimized if the solute would move to one of the stress fields created by the dislocation. Solutes that create a positive lattice dilation (larger atoms compared to the parent atoms) would position themselves on the tensile side of the slip plane, while solutes creating a negative dilation would position themselves on the compressive side. Interstitial solutes, however, move to the dilated dislocation core. While most substitutional atoms cause a purely dilatational misfit within the parent lattice, interstitials such as C or N, can induce a tetragonal distortion. An example is the tetragonal dilation of the BCC lattice along the [001] direction by carbon atoms occupying the midpoints of {001} edges [106] – which is the basis of the martensitic lattice. As solutes migrate to dislocations to assume more energetically favored positions, they form what is called a "Cottrell atmosphere" [108]. This atmosphere effectively pins dislocations, requiring additional stresses to mobilize them. Additionally, this atmosphere will predominantly be occupied by interstitials as they have greater mobility relative to substitutional atoms.

5.1.1 Solid solution strengthening in stainless steels

Most stainless steels are primarily strengthened by solid solution strengthening. Some of the alloying elements that are responsible for this are: carbon, nitrogen, molybdenum, silicon and manganese. Carbon and nitrogen, both interstitial solutes, are the most effective strengtheners, where even small amounts can drastically improve the strength [109]. However, these two elements also readily form compounds together with chromium, the main corrosion inhibiting element. Therefore, their use is limited in applications where there are strict requirements on the corrosion resistance. Substitutional solutes have a less pronounced effect as compared to the interstitials. The reason is the relatively low size misfit between the substitutional atoms and the solvent atoms. Especially the elements Cr and Ni, comprising large fractions in stainless

28

steels, have limited solid strengthening effects due to the low size misfit with Fe atoms [110], [111].

In conventional steels, carbon is responsible for the martensitic transformation, which produces a strong yet brittle microstructure that can be heat-treated to recover some of its ductility. The stainless martensitic grades are strengthened through the same mechanism, where the carbon fills the octahedral sites of the austenite lattice that during quenching transforms to the carbon saturated tetragonal body centered structure (BCT).

5.1 Grain boundary strengthening

In polycrystalline materials the individual crystals are separated from each other by interfaces. There are multiple of these interfaces with grain boundaries being one of the most important interfaces, which will be the focus of this section. Grain boundaries can be further separated into low-angle and high-angle grain boundaries. Each grain has its own crystallographic orientation, and the level of angular deviation between two neighboring grain orientations defines whether they are separated by a low-angle (≤15 °) or a high-angle grain boundary (>15 °). To accommodate the transition between two grains dislocations are formed at the interface. For low-angle boundaries a configuration of edge dislocation can easily accommodate the misorientation. However, high angle grain boundaries require more complex dislocation structures, combining screw and edge dislocations.

Grain boundaries have a pronounced effect on the strength of a material at low temperatures (T <0.5 T_m, where T_m is the melting temperature in Kelvin). The boundaries provide strong obstacles to mobile dislocations that pile-up at the boundaries when the material is mechanically loaded. Hence, leading to stress concentrations at the boundaries and eventually causing yielding of the material. There are several theories that describe the relationship between grain size and yield stress. Of the most widely known and used was described by Hall and Petch [112], [113], who formulated the following relationship:

$$\sigma_y = \sigma_0 + kD^{-1/2} \tag{13}$$

where σ_y is the yield stress, σ_0 is a frictional stress needed to mobilize dislocations, k is the Hall-Petch slope, and finally, D is the grain size. The relationship is generally valid for grain sizes between 10 and 100 µm.

A more recent theory behind grain boundary strengthening was proposed by Li [114]. Li theorized that instead of pile-up, dislocations are generated at grain boundary ledges. These are propagated further into the grain. Eventually, grains saturate in dislocations hence leading to entanglement. Meyers and Ashworth [115] proposed another mechanism, analyzing elastic and plastic incompatibility stress between adjacent grains. Due to the differences in the Young's moduli when loading a crystal lattice in the directions [100], [110] or [111], the incompatibility at the grain boundary will result in a significantly higher stress state relative to within the grain. Hence, dislocation emission will start at the grain boundary. During emission, dislocations will remain within the boundary due to the different stress states at the boundary and the grain interior, and due to cross-slip. This effectively creates a grain boundary layer that is strengthened, proving a rigid back-bone to the microstructure. At increasing stress levels, the grain interior will reach a similar stress state as the hardened grain boundary and macro-yielding will occur.

5.1.1 Grain boundary strengthening in stainless steels

Most of the stainless steels show effects of grain boundary strengthening. In the martensitic grades, it has been shown that similar relationships are in effect – albeit relating to the prior austenite grain boundary size [116], [117].

In PBF-LB processed stainless steels the cellular structure has received notable scientific attention. The cells, characterized by a cellular dislocation network with a connected solute segregation, are argued to be responsible for the relatively high strength of stainless steels processed using PBF-LB [3], [118]–[122]. Additionally, the cells have low degree of misorientation between one another and can therefore be considered as an interface, which provides a hindrance to dislocations. The cellular network is supposed to provide a soft dislocation movement moderation – increasing the strength significantly while retaining high ductility.

5.2 Precipitation and dispersion strengthening

When the solubility of an element within a phase or an alloy is exceeded, a new phase may form as a result. This phenomenon is utilized heavily in precipitation hardening, where a relatively high number density of small precipitates nucleate within the microstructure of a material. To form precipitates, the alloy must have a single-phased region within its phase diagram where all precipitates dissolve to form a solid solution. The alloy is then quenched into a region in the phase diagram where the precipitate forming elements are no longer stable as a solid solution, hence forming a supersaturated solid solution. From this state, it is possible to precipitate out the supersaturated elements in a process called aging. This is performed under controlled heat-treatments to achieve specific size distributions of precipitates. These precipitates have a similar effect to individual solid solution atoms but provide a much greater resistance to dislocations. Instead of overcoming stress fields caused by dilation of the crystal lattice, dislocations now either have to cut or loop around these precipitates in order to by-pass them [123]–[127]. Alloy systems that typically heavily rely on precipitation strengthening are the aluminum and nickel-based alloys.

Dispersion strengthening, however, relies on small, hard, and insoluble particles for strengthening. The particles are typically either intermetallics or oxides with a very high temperature stability, including Al_2O_3, ThO_2, Y_2O_3, TiC. Processing of dispersion strengthened alloys conventionally utilize PM, where the dispersoids are mixed with the base alloy powder and then consolidated. The dispersoids interact similarly with dislocations as the precipitates mentioned in the paragraph above. An advantage with dispersion strengthened alloys is that they have an extended service temperature, as the dispersoids dissolve at much higher temperature as compared to precipitates, however their strength is typically lower as compared to precipitation strengthened steels [106], [128].

The exact mechanism by which a dislocation interacts with a precipitate or particle will depend on their strength, size, and level of cohesion to the matrix phase. Cohesion is a term describing how well the crystallographic lattice of a particle matches the lattice of the matrix phase, see Figure 14 for different levels of coherency. In partial coherency, the lattice mismatch is accommodated by dislocations that form at the non-correspondence sites.
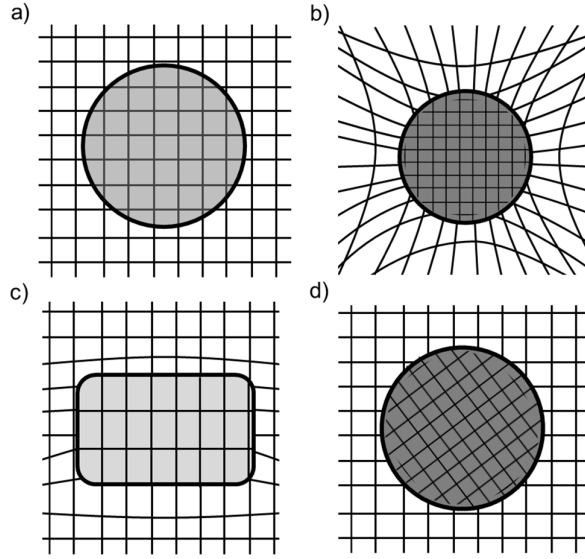
Figure 15. Different levels of coherency between a particle and the matrix phase. a) complete coherency, b) coherency but with lattice strains, c) partial coherency and d) incoherent. Re-drawn from [106].

As a dislocation approaches a particle within its slip plane, the particle will exert a force against the dislocation. Hence, for the dislocation to by-pass the particle, an additional shear stress must be applied. If the stress is sufficiently high, the dislocation will start to bow around the particle. A force balance of a dislocation bowing around a particle is given below (eq. 12), together with a schematic in Figure 16. From eq. 12 it is evident that the particle can exert a maximum force on the dislocation when $sin \, \theta = 1$. For this to happen, the particle must have sufficient strength to accommodate a force greater than *2T*. Then, the dislocation can by-pass the particle by Orowan-looping, leaving the particle undeformed, as detailed in Figure 17. If the strength of the particle, however, is below *2T* the dislocation will be able to shear the particle and pass through it. Hence, there are two possible mechanisms of dislocations interacting with particles, either through by-passing or by shearing. For an optimal strengthening effect from secondary particles, given that the interparticle spacing remains constant, the particles should be of high strength.

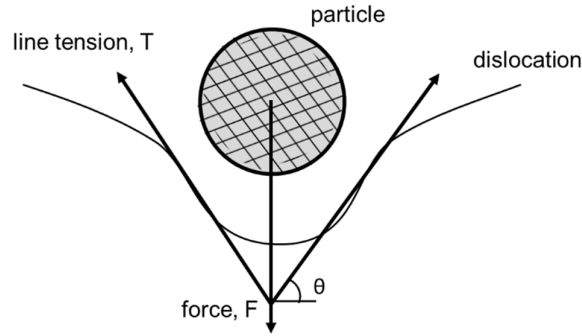$$F = 2 \, T \sin \theta \qquad (12)$$

Figure 16. Balance of forces when a dislocation is starting to bow around a particle. Re-drawn from [123].

The relative increase in strength due to particle hardening was elaborated by Orowan, and later developed further by Ashby to include aspects such as interparticle distance, and effects of statistically distributed particles [124], [128]. These equations were only regarding dislocation interactions with hard particles (where looping occurred). Particles are considered hard if they are fully developed precipitates with high strength or are incoherent dispersoids such as oxides. Soft particles are often both small and coherent with the matrix lattice. Owing to these properties, soft particles usually lack the strength to overcome the Orowan stress and will therefore be sheared when dislocations pass through them. When sheared, the ordering within the particle will be disrupted – creating either a stacking fault or an antiphase boundary, both with their own associated energies. Such faults will cause additional hindrances to dislocations. Another phenomenon of small coherent particles influencing the degree of strengthening are the strain fields created by such particles. In this case, the dislocation will arrange itself in the most energetically favorable position between the strain fields created by the precipitates, as a snake stretched across a bed of rocks. Moving such dislocation would require additional shear-stress to overcome the stress field acting upon it [106], [123].
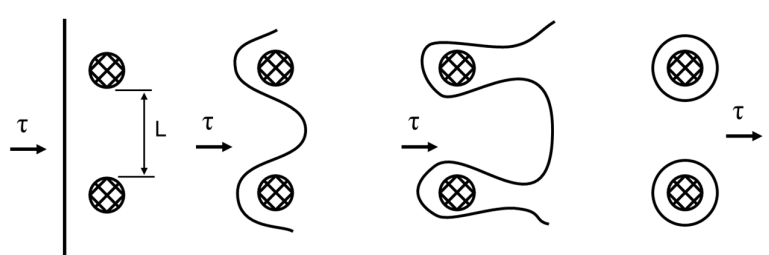

Figure 17. A schematic of a line dislocation interacting with two particles, resulting in Orowan looping. Adapted from [124].

During the age-hardening process, as the precipitates grow both in size and volume fraction, there will be different stages where the mechanisms of dislocation interaction with the growing precipitates will vary. Initially, precipitates will be sheared, then transition to the Orowan looping mechanism as the precipitates reach a critical size. The size will be dependent on the strength of the particle, where low strength, cohesive particles can grow to larger sizes before transitioning, and vice versa. At some point, the volume fraction will reach a plateau while the precipitate size continues to increase, as smaller particles will be consumed by larger particles. The driving force behind is the reduction of the interfacial area. This stage is called precipitate coarsening, or Ostwald-ripening.

5.2.1 Precipitation and dispersion strengthening in stainless steels

There are numerous stainless alloy groups that utilize dispersion or precipitation strengthening. Of the commercially available dispersion strengthened alloys are the MA956 and PM2000 grades [129], both utilizing oxide dispersions for strengthening (ODS). Out of the precipitation strengthened steels are the Cu-precipitating alloys 17-4PH and 15-5PH, and the Ti, Al and Mo forming alloys including: 13-8Mo and Custom 456®, forming NiAl and η-Ni_3Ti, respectively. Finally, the alloy Nanoflex® combines the precipitation of Cu with γ'-Ni_3(Ti, Al, Si) and η-Ni_3Ti [130]. Both, ODS and precipitation strengthened steels have been investigated within the thesis, hence a more careful introduction will be presented below.

The ODS steels incorporate nanometric Y_2O_3 or Y-Ti-O oxides due to their high thermal stability and strength to achieve a dispersion strengthening effect [131]–[133]. The ODS steels are primarily ferritic or martensitic, as the intended application areas are within the nuclear industry – where excellent thermal conductivity and minimal thermal expansion are sought after [134]. The use of dispersed oxides extends the service temperature of ODS materials to 800 °C, as opposed to 550-600 °C of the conventionally used Cr-steels [129], [134], [135]. The ODS steels have a complex PM processing route, where oxide and base-alloy powder is extensively ball-milled to produce <10 nm oxide distributions with number densities in the range between 10^{20} and 10^{24} m^{-3} in the final microstructure [129]. The mixture is compacted followed by hot extrusion into a bar, and subsequently rolled into thin sheets. The complex processing route combined with issues of dispersion homogeneity has limited the full commercialization of such alloys.

The precipitation strengthened stainless steels are mainly martensitic, hence the name maraging – combining the words martensitic and aging. The martensite phase, with its highly dislocated structure, provides high density of nucleation sites to ensure a homogenous precipitation process [136]. As opposed to a carbon-rich martensite, the martensite formed in maraging steels is mostly free of carbon, making it ductile. Thus, the alloy group is frequently used in applications where high formability and weldability in combination with high strength is required. The relatively high ductility in the un-aged state has also made this class of materials highly suitable for PBF-LB [137].

6. Experimental methods

This chapter aims to provide a brief overview of experimental methods and techniques applied for powder characterization, sample manufacturing, testing and characterization.

6.1 Powder characterization

To properly characterize the powder grades in *Papers I* through *III*, several techniques had to be employed. Initially, to verify the sieving efficiency and accuracy the particle size distribution is measured by laser diffraction. By irradiating a powder sample with a laser, the interaction between the laser beam and the powder particles causes the laser beam to scatter, and this scattering is detected by a detector. This scattering will be dependent on the particle size, hence producing a particle size distribution (PSD) curve. For the analysis, a Sympatec HELOS with the dry disperser RODOS was used.

Conventional flowability and powder densities were evaluated using with Hall-flow, apparent and tap density at 4000 taps. The methodology as described in the ISO 4490:2018, 3923-1:2018 and 3953:2011 standards were used for the testing, respectively.

Additional flowability measurements were performed using a powder rheometer (Freeman FT4) and a revolving drum analyzer (Revolution Powder Analyzer, Mercury Scientific). Using the Freeman FT4, the standard stability and rate sensitivity tests were run – consisting of 8 tests using a constant speed of the impeller followed by 3 tests with incrementally slower impeller speed. Flowability and multiflow tests were run using the Revolution Powder Analyzer. Flowability was measured by evaluating the avalanches as a constant RPM of 0.6 min^{-1} while the multiflow tests were conducted by incrementally increasing the RPM up to 70 min^{-1}. In all the tests, 25 ml of untapped powder was used for the evaluations.

6.2 PBF-LB process

In this work an EOS M290, located at Chalmers University of Technology, was used for printing. It is equipped with an Yb-fiber laser source operating at a maximum power of 400 W and a laser spot size of 80 µm in diameter. The machine features a build area of 250 x 250 mm^2 and a maximum build height of 325 mm. All the powder that was used in the investigations was supplied by Höganäs AB and delivered in both 20-53 µm and 15-45 µm sieve fractions.

Samples for *Paper II* were built using standard parameters, 316 L_SurfaceM291 1.10 and 316 L_040_FlexM291 1.00 (20 and 40 µm layer thickness, respectively), and in-house developed parameters for 60 and 80 µm layer thicknesses. For *Paper III* and *IV* samples were printed using the standard 316 L_SurfaceM291 1.10 parameter. In *Paper V* the standard 40 µm parameter for MS1 was used, MS1_ 40_PerformanceM291 2.0. The samples built for *Paper II* and *V* were built using a reduction module due to the low amount of available powder.

Prior to initiating the print, the machine was purged using Ar gas with a 5.0 purity until an oxygen level of 0.1% was reached.

6.3 Sample preparation

To investigate the printing performance of the different powder grades as well as their microstructure, printed cubes had to be sectioned and prepared for light and electron microscopy. A general overview of the sample preparation procedure with the conducted

investigations is presented in Figure 18. Sectioning of the cubes were done parallel and perpendicular to the building direction. Samples were then mounted in a thermosetting resin followed by grinding and subsequent polishing. The general procedure is outlined below:

- Plane grinding using SiC until flat
- Fine grinding using 9 μm diamond suspension
- Polishing on napped cloths using 3 and 1 μm diamond suspensions
- Final polishing using 0.04 μm colloidal silica suspension

Apart from cubes, samples for metallographic investigations were also prepared from tensile test bars. The tensile bars had previously been pre-tensioned, and sectioning was done from the center of the gauge section. The procedure outlined above was used to prepare samples.

The *as-polished* samples were investigated using light optical microscopy, details of which can be found under subsection 6.4.1. Additionally, the *as-polished* samples were tested for hardness using Vickers hardness.

To reveal the microstructure the samples were either chemically or electrolytically etched. Electrolytical etching was employed in *Paper II* through *IV* and was performed using a 10% water-based solution of oxalic acid, under a 3 V potential. While chemical etching was used in *Paper V* through immersion in Kalling's II solution.
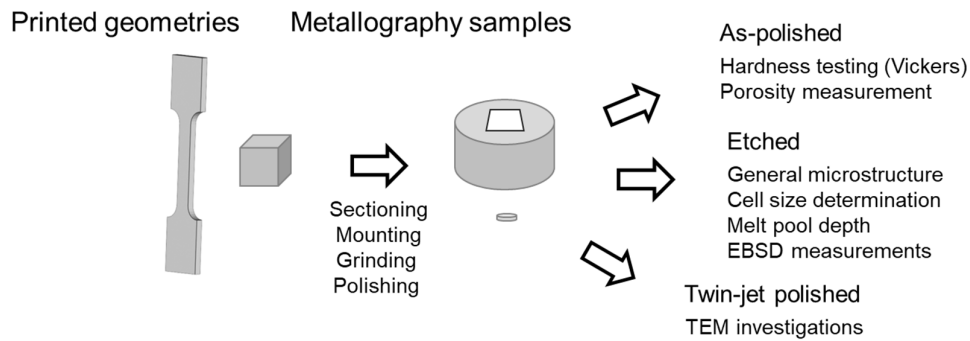

Figure 18. An overview of the sample preparation process used in this work.

Additionally, thin-foils for transmission electron microscopy were prepared by sectioning thin sections from printed geometries. These were further thinned by mechanical grinding using SiC paper until they reached a thickness of ~100 μm. Following the grinding, the thin section was electrolytically twin-jet polished using a 10% perchloric solution that was cooled to -30 °C.

6.4 Analysis Techniques

6.4.1 Light Optical Microscopy (LOM)

Throughout this thesis study, a Zeiss Axio Imager M2M and a Zeiss Axioscope 7 were used to capture polished and etched images for porosity measurements and microstructural characterizations. The microscopes were equipped with an automatic stage, enabling cross-sections to automatically be stitched from a series of high magnification images.

Images for porosity measurements were further analyzed using the Fiji distribution of the imageJ software [138]. Images were cropped to include only the bulk and made binary (black

and white) through an automatic thresholding operation (using the default algorithm). The use of an automatic method was chosen to reduce user bias and to increase the repeatability. The thresholding operation determines what gray-value should be considered the cut-off for the two classes. Therefore, images of samples that belong to a series should preferably be documented under one session to ensure equal illumination and exposure settings. To quantify the pores/defects (both appear with a dark contrast and will be put into one class) a particle counter within Fiji was utilized – rendering an area fraction between the two classes.

6.4.1 Scanning Electron Microscopy (SEM)

A SEM is a common microscopy tool for characterization within many scientific fields due to its high resolution, versatility, large depth of field, and ease of use.

The image is produced through an interaction of the specimen with a focused electron beam accelerated to high voltages (up to 30 kV). The electrons are generated either through tungsten or LaB$_6$ filaments on the one hand or field-emission emitters on the other. The resulting resolution depends on the electron source, with the field emission gun (FEG) providing the brightest yet most narrow beam, optimizing the resolution. The beam is focused and scanned over the surface of the sample through an array of magnetic lenses. As the electrons hit the surface of the sample, they interact with the electrons within the sample down to a depth of around 1–2 µm. The exact depth depends on the acceleration voltage, the atomic density of the illuminated feature and the angle of the incident beam. The interaction is basically a scattering of the incoming electrons as they hit the sample surface, which can be both inelastic and elastic. Elastic scattering (BSE) occurs when the incident electron interacts with the nucleus of the sample atom, bending its trajectory. Inelastic scattering occurs when the incident electron collides with the atom and transfers some of its energy to it. The two interactions are illustrated in Figure 19, which also shows the depths where the interactions occur.
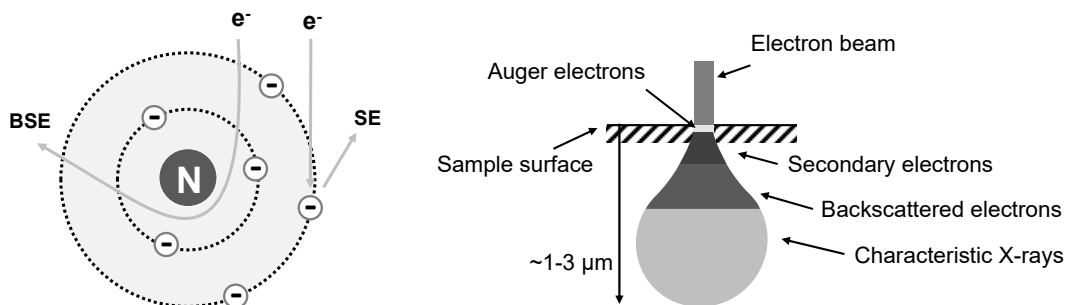

Figure 19. Schematics of incident electron interaction (left) and the interaction volume (right).

As the incident electron transfers its kinetic energy to the loosely bound outer-shell electrons, some escape from the atom as secondary electrons (SE). The emitted SE has a low kinetic energy, ~50 eV, and thus escapes from the surface of the sample. SE provide topographic contrast from the sample surface and is the most commonly used imaging method. If, however, a greater amount of the energy is transferred to the inner-shell electrons, an inner-shell electron can be knocked off. This creates an electron hole that is filled by an outer shell electron, and this transition creates characteristic X-rays. These can be further used for chemical analysis in the SEM [139].

In this work, powder and etched microstructures were studied in a LEO Gemini 1550 FEG-SEM equipped with an X-Max EDX detector.

6.4.2 Electron Backscatter Diffraction (EBSD)

Electron backscatter diffraction is a crystallographic characterization technique that is used in conjunction with SEM. This technique enables a highly localized analysis of the crystal structure, grain orientation, phases, and strains in a crystalline sample. EBSD makes use of the backscattered electrons, or BSE, that emanate from the top surface of the sample. Some of the BSE simultaneously fulfil the Bragg condition due to the interaction with the crystallographic planes within the sample. This diffraction event causes two Kessel cones per lattice plane to form. These cones can be imaged using a phosphor screen. Together, these two cones form a Kikuchi-line, see Figure 20. Several diffracting planes form multiple lines and together they create a diffraction pattern, which is recorded by a camera within the EBSD detector. Typically, diffraction patterns have relatively weak intensity. Therefore, the sample needs to be tilted 30 ° relative to the incident beam, or 70 ° relative to the horizon to improve the intensity of the Kikuchi-lines.

As the Kikuchi-lines form due to diffraction of the electrons with the crystallographic planes, their width contains information about the lattice spacing of the diffracted plane. The angles between several Kikuchi-lines provide information on the crystal structure. The intersections between multiple Kikuchi lines correspond to a zone axis, or pole, and they indicate the crystallographic directions. Combined they provide information on the crystal structure and how it is oriented relative to the sample.
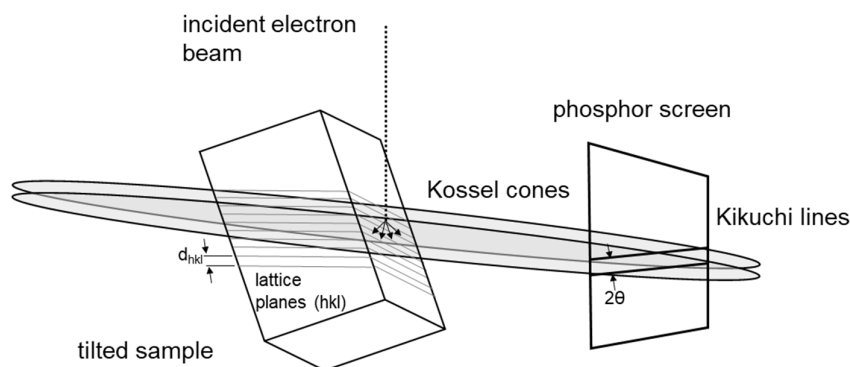

Figure 20. Schematic of the formation of Kikuchi lines. Re-drawn from [139].

In the present work, EBSD was used for phase identification, grain analysis and for the analysis of strains. In *Paper III* evaluation of the grain size was done with EBSD, as grain delineation has proven difficult using conventional techniques such as etching combined wiht LOM or using BSE detectors in the SEM. Grain boundary maps were constructed from EBSD maps using the HKL Channel 5 software (Oxford Instruments) and defined according to a misorientation of >15 °. Due to the irregularity in grain morphology, the mean lineal intercept method [140] was found to produce the best results for size determination. Local plastic strains cause dislocations to pile up, and this can be detected by EBSD as these cause minor misorientations of the crystal [141]. *Paper III* used kernel average misorientation maps, KAM maps, to detect strains that are accumulating at the cell walls. The KAM maps are constructed on the basis of a pixel's degree of misorientation relative to its neighboring pixels, also called

a kernel [141]. A threshold of 2 ° was used to avoid the influence of sub-grain boundaries. The maps were created using the HKL Channel 5 software. Finally, EBSD was used to check for austenite formation or reversion in *Paper V.*

The data was obtained using Nordlys II and Symmetry S1 (Oxford Instruments) detectors using an accelerating voltage of 20 keV and a step size of 0.08 μm. Analysis was performed using the HKL Channel 5 software and the MTEX toolbox [142].

6.4.3   Transmission Electron Microscopy (TEM)

In transmission electron microscopy, an electron beam is accelerated to voltages between 100 kV and 300 kV and irradiates a thin sample. The electrons are generated and focused in a similar manner as in the SEM, with some instruments allowing similar scanning of the beam (STEM). As compared to SEM, in TEM, the wave characteristic of the electron is taken advantage of for the imaging, and as such, the resolution of the TEM can be much higher. As the beam passes through the sample, it interacts with it and forms an image. For the beam to be able pass through the sample, it must be electron transparent, and hence, samples must be very thin, below <100 nm. The image is focused and magnified, then projected onto a fluorescent screen, which produces a viewable image. Contrast is generated through changes in the amplitude of the electron wave as it passes through the sample. Amplitude changes can occur due to variations in the thickness (or density) in the sample, creating a variation in the scattering. The diffraction contrast also influences the amplitude of the electrons. Depending on the crystal structure and its orientation, the electrons will be scattered differently and produce contrast changes.

Another feature of the TEM is the ability to analyze the crystal structure of specific constituents of a microstructure within a sample. As the electrons behave as a wave, when they pass through the sample the atoms in the sample act as a diffraction grating. Thus, a diffraction pattern forms and can be used to calculate lattice parameters [143].

In this work, two TEM microscopes were used: an FEI Titan operating at 300 kV and an FEI Tecnai T20 operating at 200 kV. Both were equipped with EDX systems and capable of running in STEM mode.

6.4.1   Atom Probe Tomography (APT)

Atom probe tomography is a microscopy technique with a very high spatial resolution (<0.3 nm) that allows for a three-dimensional analysis and visualization of millions of atoms within a sample [144]. APT has the capability of detecting all elements in the periodic table, with equal and high sensitivity. Making this technique very suitable for the analysis of small precipitates.

The working principle behind APT is the field evaporation of atoms from a thin needle sample (radius of <50 nm) by the means of a very high electric field. The high electric field, which is created using a voltage of 2 to 10 kV, sets a baseline field that is close to the field required to evaporate an atom. To overcome the bonds of individual atoms and to produce an evaporation event, the needle is subjected to a voltage or laser pulse. The field required for an atom to evaporate will also be dependent on the element and its bond to its neighboring atoms, for example the field required to evaporate atoms from a precipitate may be higher relative to its matrix. Once the ionized atoms escape the sample, they are accelerated by electrostatic forces

before hitting the detector. The magnification achieved by APT originates from the ion trajectory from the sample to the detector, and it is dependent on the local curvature of the APT needle. The detector records both the *xy*-coordinates and the time-of-flight of the ion. The time-of-flight is used to calculate the mass-to-charge ratio, which is used to identify what element formed the ion. To limit aberrations and several ions hitting the detector simultaneously, the needle is typically cooled to around 20-50 K [144], [145].

Atom probe tomography was utilized in *Paper V* to analyze the density, size and composition of precipitates within a maraging steel. The experiments and analysis were exclusively performed by Assoc. Prof. Mattias Thuvander. The atom probe was a LEAP 3000X HR (Imago Scientific Instruments), which has a detection efficiency of 37%. The analyses were made in laser pulse mode, with a laser wavelength of 532 nm at a pulse frequency of 200 kHz, laser pulse energy 0.30 nJ, sample temperature 50 K and evaporation rate 0.20%. The reconstructions were made using the voltage method, with an image compression factor of 1.65, a field factor of 3.0-4.0 and an evaporation field of 25 V/nm. Iso-concentration surfaces (isosurfaces) were obtained using a cubic voxel size of 1.0 nm^3 and with delocalization of 3x3x1.5 nm^3. The statistical tools radial distribution function (RDF) [146] and maximum separation method (MSM) [147] were used to study co-precipitation tendencies and early clustering, respectively.

6.4.2 X-ray Photoelectron Spectroscopy (XPS)

X-ray photoelectron spectroscopy (XPS) is a surface-sensitive analytical method for chemical analysis with the ability to resolve chemical states within a sample, for example, if Fe is present as an oxide or as a metal. It probes up to 10 nm of the surface. X-ray photoelectron spectroscopy is not limited to certain elements, and thus, all elements except He and H can be successfully detected and quantified.

The working principle is that an X-ray beam irradiates a sample and the irradiation causes the atoms within the sample to ionize. During the process of ionization, the sample atom releases photoelectrons, which are detected by the XPS. The photoelectrons have a certain kinetic energy as they are emitted, and the energy is dependent on several factors, such as the element that emits the photoelectron, the specific electron orbital and the chemical bonding. The emitted photoelectrons are focused and analyzed in a hemispherical analyzer, which quantifies the kinetic energy of the electrons. The data is presented as the number of counts as a function of the binding energy (BE). The BE relates to the recorded kinetic energy according to the following equation:

$$E_B = h\nu - E_K - \Phi \tag{14}$$

where E_B is the BE, $h\nu$ is the energy of the incident X-ray photon, E_K is the kinetic energy and Φ is the spectrometer work function of the system.

In this study, a PHI 5500 with a monochromatic Al K_α X-ray source was used for analyzing the surface oxides of 316L powder. Survey spectra were collected using 93 eV pass energy, with a 0.4 eV step. Narrow scans of elements of interest were collected at 23.5 eV pass energy and a 0.1 eV step. The energy calibration of the system was performed using pure elemental standards of Ag, Au and Cu. The etch rate was calibrated using a Ta foil with electrochemically grown Ta_2O_5 with a defined thickness of 100 nm; therefore, all of the etch depths are related to the etch rate of Ta_2O_5.

6.4.3 Mechanical testing

Test coupons for impact testing were built according to the geometry as described in the standard ISO 148-1 (Charpy V-notch). Most tensile test specimens were built according to ISO 2740, however both miniature and specific elevated temperature geometries were used too. All geometries are shown below in Figure 21.
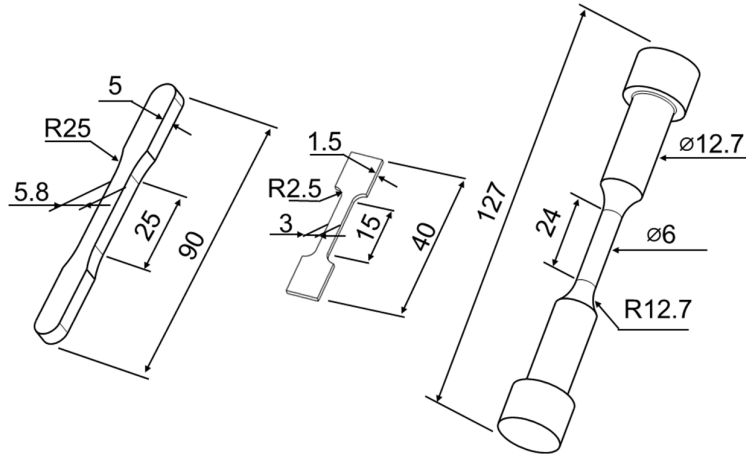

Figure 21. Technical drawings of the geometries used for tensile testing. From left to right: ISO 2740, miniature and elevated temperature test geometry.

The impact toughness was tested using a 150 J anvil and performed according to the standard ISO 10045-1 using an Instron Wolpert pendulum tester. Similarly, ambient temperature tensile testing was performed according to the ISO 6892-1 standard using Zwick Z100 and Instron 5500R tensile testers. The testing was conducted under strain-rate control. For tests at elevated temperature the testing was conducted according to the ASTM E21 – 17 standard, the heating was done in a three-zone split furnace and the temperature was controlled through a contact thermo-couple.

Hardness was measured using a Vickers pyramid diamond indenter using a load of 5 kgf. The hardness testing was performed on a Struers DuraScan 70-G5. The reported values were an average of 5 indentations.

7. Summary of appended papers

7.1 316L powder properties

Effect of atomization on the surface oxide state of 316L powder

316L stainless steel powder was atomized using different atomization practices to compare the influence of atomization on the surface oxide state. Specifically, powder produced using VIGA (argon atomized), CGA (nitrogen atomized), and WA were investigated. The purpose was to establish a base-line of the VIGA powder so that a comparison relative to the other grades could be made.

Initial powder investigations of the surface using electron microscopy, see Figure 22, revealed that the surfaces of the VIGA powder were relatively clean. Despite this, some nanometric oxide particulates could be detected in the inter-dendritic areas of the powder surface – with a morphology that resembled a splat. The CGA powder had similar features, yet also had distinct hemispherical features that appeared with a dark contrast when imaged in the SEM. The presence of oxide particulates, that were both larger and more frequently appearing, were noted on the surface of the WA powder. Some of the flake-like oxide particulates on the WA powder appeared to have relatively low cohesion to the powder surface – as they seemed to be protruding from the powder surface. From a visual examination, the presence and size of oxide particulates were the least in the VIGA powder, and the most in the WA powder.
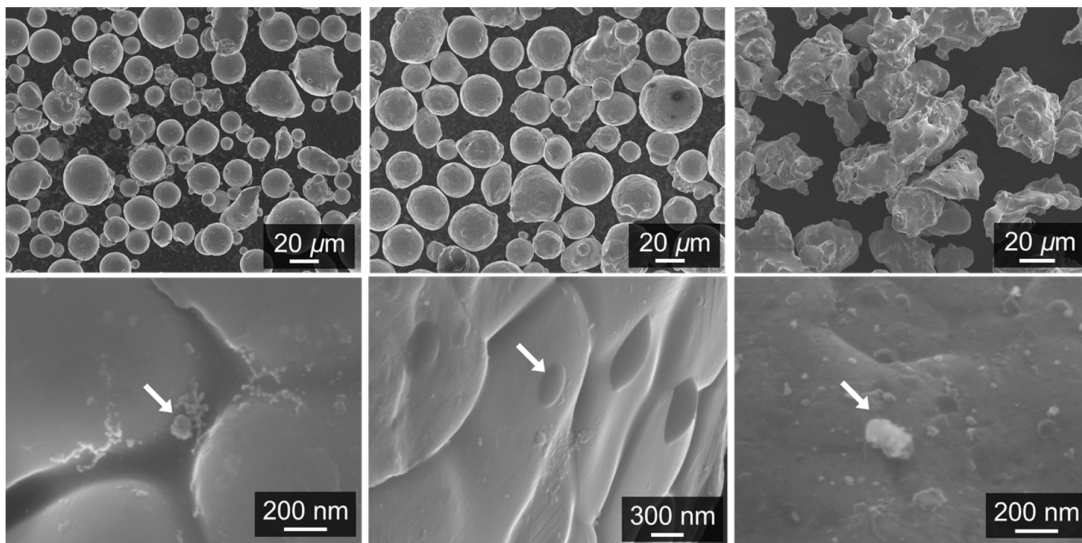
Figure 22. SEM micrographs in low and high magnification of investigated 316L powder. From left to right, VIGA, CGA and WA. Characteristic oxide particulates are highlighted with arrows. Reproduced from [148] under CC BY 4.0.

The XPS analysis revealed that, in the gas atomized grades, Cr, Fe, Mn and O were the major elements found on the powder surface. These metallic elements were found in their oxide state, with similar peak positions for the VIGA and CGA grades. The surfaces of the CGA powder had also a discernable peak of oxidized Si. The analysis of the WA powder revealed that the surface oxide layer was predominantly consisting of Si-based oxide, including minor quantities of Fe and Cr. Fe, Si, and O had shifted significantly to higher binding energies in the case of the WA powder. The positions did not satisfactory match those of known oxides – indicating

possible hydroxide or spinel formations. Based on previous knowledge of powder oxidation during atomization, it was hypothesized that the elements Cr, Mn and Si were present in the form of oxide particulates, while Fe was present as a thin surface oxide between particulate islands. An EDS analysis across larger particulate features confirmed that they were enriched in the suggested elements.

Depth profiling further confirmed the hypothesis, where the relative cation concentrations of Cr, Mn, and Si were progressively increasing as Fe was decreasing (see Figure 23). Hence, the thin Fe-oxide layer was effectively sputtered away while the particulates remained deeper throughout the profile. Both, VIGA and CGA displayed similar profiles. In the WA powder, the cation depth profile, in Figure 23 c), suggests that Si could also be present as a thinner surface oxide layer. Finally, the Fe-oxide layer thickness was evaluated using the relative Fe-intensity, see Figure 23 d). It was found that the thinnest Fe-oxide layer was on the WA powder at 3.2 nm, while VIGA and CGA had a surface oxide layer of 4.1 and 4.0 nm, respectively. The very thin layer Fe-oxide on WA could provide additional clues to that Si might also be comprising the surface oxide layer.
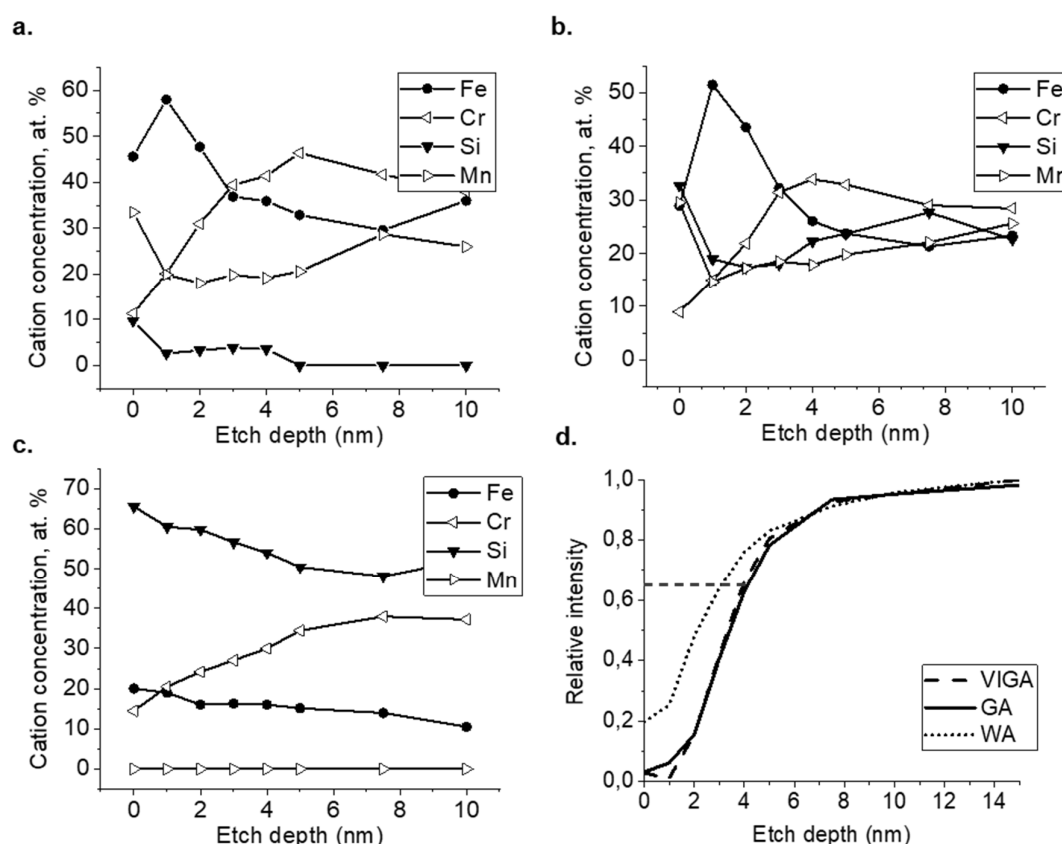

Figure 23. Calculated cation concentrations of oxides found on the surface of a) VIGA, b) CGA, and c) WA. d) Relative intensity of the Fe-metallic peak, allowing for a calculation of the oxide layer thickness. Reproduced from [148] under CC BY 4.0.

As a concluding remark, it was found that differences between the gas atomized powder grades were minimal, if not negligible. Thus, the use of CGA powder in the PBF-LB process should not have any detrimental effects on processing and final mechanical properties – based on the surface oxide state alone. However, this does not regard other powder properties such as

flowability. Finally, the surplus of oxygen in the WA powder does not originate from a thicker oxide layer that forms during atomization, rather it is due to its much higher surface area.

Effects of powder flowability on PBF-LB processing

After establishing the effects of atomization on the surface oxide state, the implications of the physical powder properties on PBF-LB printability were to be investigated next. The investigation continues with the same powder grades as in those reported in *Paper I*, including a modified version of the WA powder.

Flowability measurements for AM have still not fully evolved to the point where one can state what powder properties are the most important for good processability. Within that context, the term spreadability is often mentioned. As powder spreads rather than free-flows in PBF-LB, it is important to find flowability indicators that best replicate the stress-state of powder when it is spread. Therefore, several different methods for powder characterization were evaluated. These included traditional PM methods such as Hall-flow with apparent and tapped densities, the Freeman FT4 powder rheometer, and finally the revolving drum analyzer, Revolution Powder Analyzer (RPA).

The flowability analysis revealed, like the findings of *Paper 1*, that the two gas atomized powder grades tested very similar throughout most of the testing methods. The WA grade, however, displayed significantly lower flowability and density values as compared to the CGA and VIGA grades. This can be attributed to its highly irregular morphology, causing individual particles to interlock with each other. Finally, the modified WA grade, abbreviated as WA-M, performed as an intermediary between the gas atomized grades and the WA grade. In Hall-flow testing, this powder showed better flow as compared to the CGA grade, see Table 2

Table 2. PM flowability evaluations of the tested powder grades.

Grade	AD (g/cm^3)	TD (g/cm^3)	Flow (s/50g)	x_{10} (µm)	x_{50} (µm)	x_{90} (µm)
VIGA	4.4 ± 0.01	5.1 ± 0.03	15.9 ± 0.1	18.1	31.1	52.0
CGA	4.3 ± 0.01	4.9 ± 0.04	18.1 ± 0.3	26.1	42.2	63.3
WA	2.4 ± 0.01	3.1 ± 0.02	37.4 ± 0.6	25.8	46.5	70.4
WA-M	3.7 ± 0.03	4.6 ± 0.02	16.4 ± 0.1	24.9	41	58.8

The data produced by the FT4, and RPA (see Figure 24) contained some findings that might be counter-intuitive. Starting with the FT4, only the standardized (by the machine supplier) stability and rate sensitivity tests were run. While the basic flow energy (BFE) showed results that correlated with the PM flowability evaluations, the specific energy (SE) showed highest energy for VIGA powder, followed by WA, and WA-M. As SE is measured on the upward stroke of the impeller, it should replicate spreadability relatively well, as the flow is not confined and provides a measure of the cohesive properties. The results were not found to correlate with the other findings. Regarding the RPA, the difficulty lies in finding what properties to consider. Most frequently, the avalanche energy (AE) together with the avalanche angle (AA) are presented. Though in this study, none correlated with any previous result, both from FT4 and PM methods. Despite this, there was an RPA property that provided results that

were consistent with the other findings of this study, which was the break energy (BE). As seen in Figure 24 b), it measures the VIGA and CGA grades nearly identically, while the WA grade has higher reported energy values.
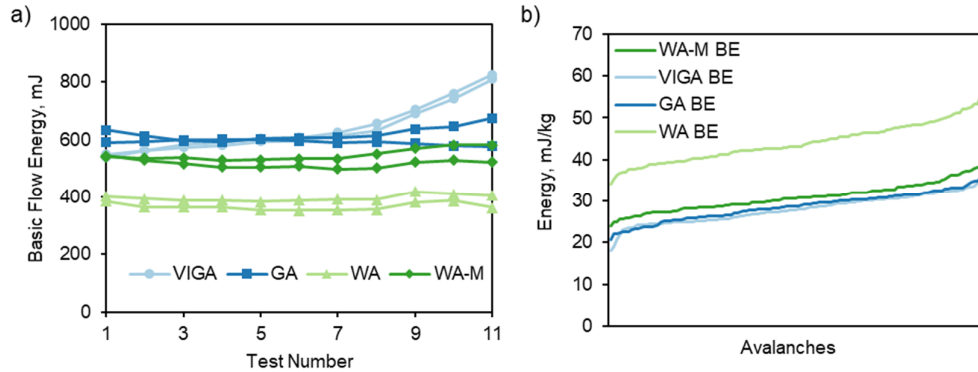

Figure 24. Powder flowability evaluations by a) FT4 and b) RPA. Reproduced from [55] under CC BY 4.0.

The powder grades were then printed in the M290 at various layer thicknesses, see Figure 25. Using 20 µm, there was no statistically significant difference between the different powder grades. However, above 20 µm the ability to print to full density deteriorated for the two WA grades, yet the modified grade performed significantly better up to 60 µm. For the gas atomized grades, VIGA performed marginally better at 40 and 80 µm layer thicknesses.
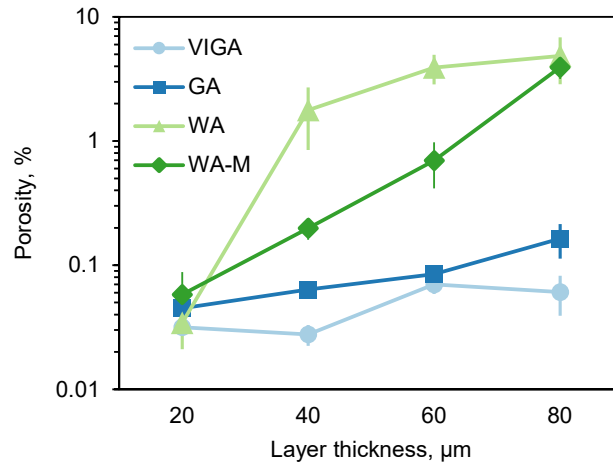

Figure 25. Results from the printing trials at various layer thicknesses. The residual porosity is shown as a function of the layer thickness. Note the logarithmic scale on the y-axis. Reproduced from [55] under CC BY 4.0.

Connecting the findings with the powder properties revealed that powder flowability does not fully dictate the performance of a powder grade. A seemingly important property was found to be the powder density, which all methods were able to differentiate correctly and correlated closely between each other. As perhaps not surprising, a single powder property was not able to predict the printability. Rather, high printability can be achieved if a set of properties are fulfilled, e.g., high relative powder density, low break energy and high Hall-flowability. However, these properties are all, to some degree inter-linked. The study also showed that both

46

the FT4 and RPA can adequately characterize powder suitability for PBF-LB, and did so better than Hall-flowability. Although the property selection has to be carefully scrutinized.

7.2 Strengthening mechanisms of PBF-LB produced 316L

Cell structures, their thermal stability, and their interaction with dislocations

When processed with PBF-LB, the stainless steel 316L has shown consistently higher strength values as compared to when it is processed conventionally, while simultaneously retaining its ductility. Hence, drastically improving the strength-ductility trade-off. The reason for this improvement of properties is the development of a unique cellular structure. This cellular structure consists of walls containing extensive dislocation structures. Additionally, the segregation and enrichment of both, Cr and Mo have been found at the dislocation structures. This combination of thick dislocation tangles and elemental segregation provides a soft dislocation pinning, where mobile partial dislocations get trapped. While the cellular network significantly increases the strength, it also decreases the work hardening rate – an important feature of engineering materials. To regain some of the work hardening the alloy usually undergoes heat treatment. Yet, the full thermal stability of the cellular network and how the heat treatment affects dislocation interactions has not been fully investigated. Therefore, we investigated the cellular network as a function of different heat treatments on the ability for the cells to accommodate strain.

From SEM investigations it could be seen that the cellular networks began to dissolve at about 800 °C, while full dissolution was observed at 1200 °C. At 800 °C, few dislocations remained at the cellular walls as observed by TEM, see Figure 26. Yet, when performing line-scans over the cellular walls by EDX in the TEM, the compositional segregation that had been present in the as-built state had annealed out. Additionally, the cell size remained constant up until the dissolution of the cells. The grain size was also evaluated as a function of the heat-treatment temperature. The grain size increased only at 1200 °C, with KAM maps of the microstructure revealing that only partial recrystallization had occurred. Hence, suggesting that PBF-LB structures require elevated temperatures and times to fully recrystallize.
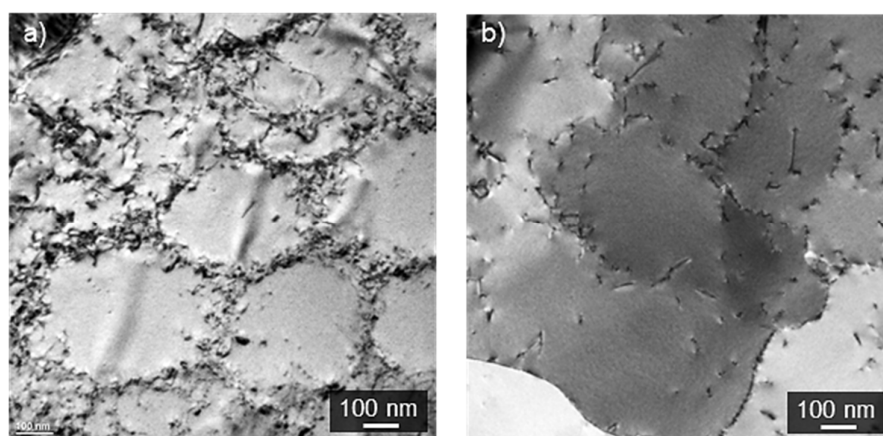

Figure 26. TEM micrographs of the cellular network in the a) as-bult condition and b) heat-treated at 800 °C.

The strain accommodation ability of the cellular network after the heat-treatments was evaluated by investigating the cells in both unstrained and pre-strained conditions. By utilizing

high-magnification KAM-maps, it was possible to quantify the local strain accumulation. In the unstrained as-built condition, considerable misorientation was detected at the cell walls. Hence strain had accumulated there, see Figure 27. The case was similar when the structure was heat-treated at 400 °C, yet the relative frequency of the local misorientation histogram had shifted somewhat to lower degrees. Hence, already at 400 °C relaxation is active. After treating at 800 and 1200 °C, no clear misorientation at the cellular walls was detected.

After straining the specimens, the KAM maps showed an increased local misorientation around the cell walls in the as-built samples and the sample heat treated at 400 °C. The local misorientation histograms shifted to higher degrees, hence strain was accumulating there. Surprisingly, weak strain accumulation was also detected in the sample heat-treated at 800 °C, see Figure 27. Hence, even when the cellular network had almost fully been removed, the low density of dislocations were still able to provide resistance to dislocation glide.
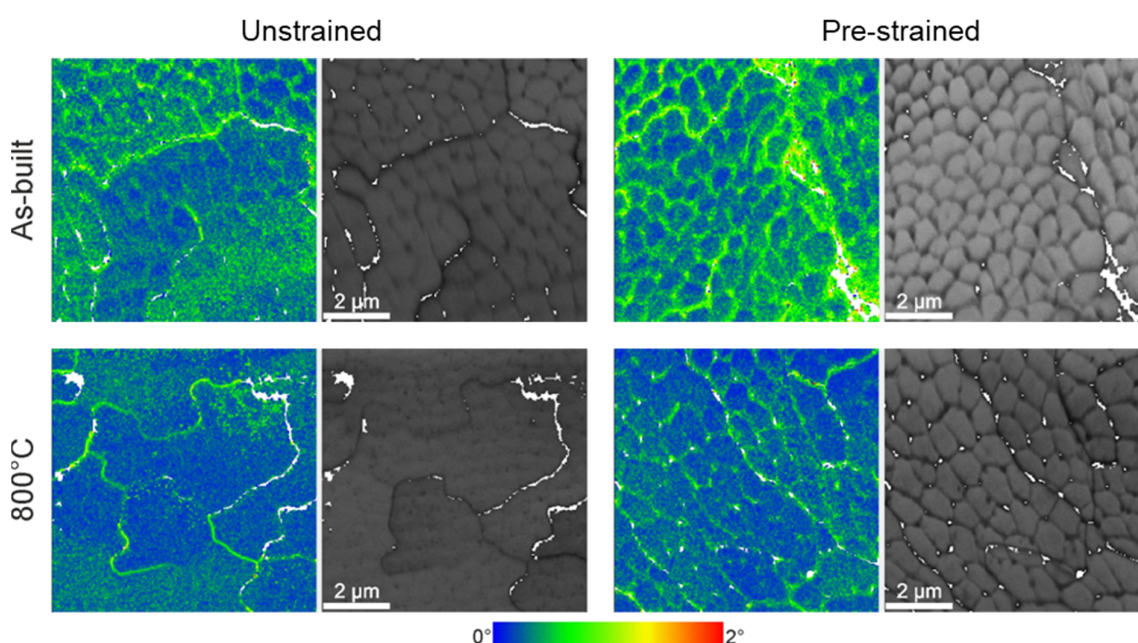

Figure 27. KAM and band contrast images of unstrained and strained samples in the as-built and heat-treated at 800 °C conditions.

The above observations were further confirmed by mechanical testing, presented in Figure 28. In conditions where the cellular walls were relatively saturated with dislocations, the resulting strength was high. However, it comes at the cost of limited strain hardening ability and a minor decrease in the ductility. Conditions that lacked the extensive dislocation structure at the cell walls, exhibited an increasing strain hardening ability yet at the cost of decreasing yield strength. Finally, when measuring the area reduction of cross sections in tensile specimens, it was found that the as-built and the samples heat-treated at 400 °C had higher area reduction. Hence, despite having lower total elongation to fracture the elongation at the neck was greater – accentuating the ability of cellular networks to strengthen the material, while also retaining high ductility.
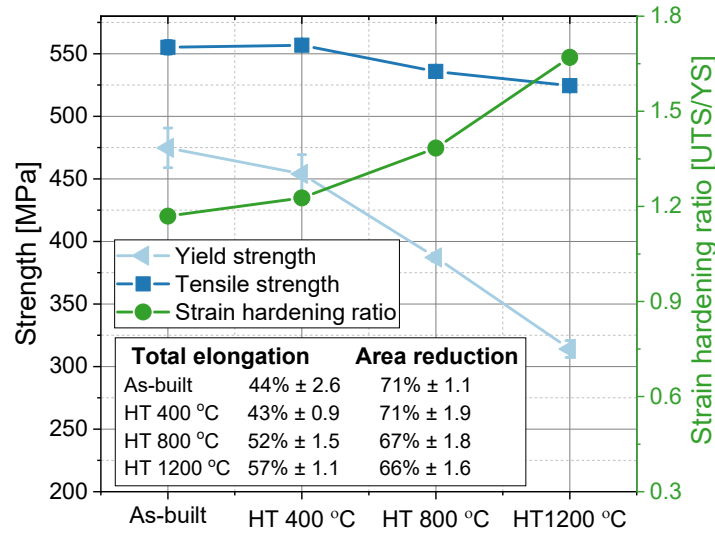
Figure 28. Mechanical testing of the different conditions of PBF-LB processed 316L. Reproduced from [149] under CC BY 4.0.

7.3 Methods of improving the strength of stainless steels further

In-situ oxide dispersion strengthening of 316L

The study evaluated the concept of in-situ oxide dispersion synthesis using WA 316L powder. The conceptual idea was formulated when researchers reported of nanometric oxides in PBF-LB processed materials when using VIGA powder grades. ODS steels contain typically between 0.15 and 0.35wt.% oxygen to achieve high volume fractions of oxide dispersoids. Typically, VIGA or CGA powder usually contains below 0.05wt.% oxygen, while WA powder contains between 0.2 and 0.4wt.% of oxygen. Hence, by increasing the amount of oxygen during processing the volume fraction of dispersoids could be increased.

Samples from CGA and WA powder grade of the alloy 316L, those that had been investigated in *Paper I & II*, were processed using PBF-LB. The samples were studied in SEM and TEM to quantify presence of oxide dispersoids. The oxide dispersoids were fully spherical and were homogenously distributed throughout the microstructure, hence no agglomeration or segregation to cell walls was present. After sizing and counting, the average dispersoid sizes were shown to be 46 and 56 nm in the CGA and WA samples, respectively. A box plot is shown in Figure 29. The number densities were 1.3 x 10^7 and 1.6 x 10^7 mm^{-2} in CGA and WA samples, respectively.
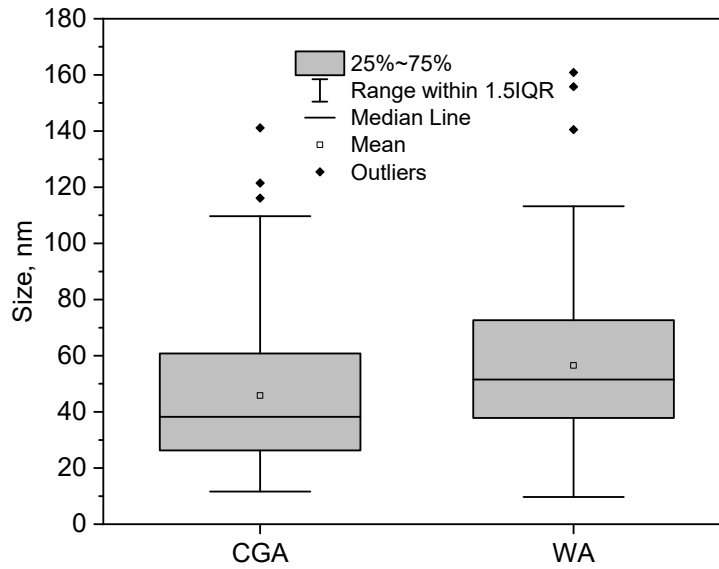
Figure 29. Box plot of the dispersoid distributions for PBF-LB processed samples made with gas-atomized (CGA) and water-atomized powder (WA).

Mechanical testing of the two materials, both at room temperature, and at 550 °C, showed no strength advantages of having an increased oxide volume fraction as found in WA. However, the gap between the CGA and the WA materials significantly reduced at 550 °C.

As the powder state of these powder grades was extensively studied in *Paper I,* it is possible to elaborate on the powder-to-sample oxide transformation. EDX analysis of the oxides in as-printed material is provided in Figure 30. Relative to the surface oxide state, CGA oxides had reduced to mainly a Si-based oxide. For the WA material, the oxide particles seemed also to decrease in size relative to the surface particulates. The oxide transformation could be explained through thermodynamics. As the particulates melt in the melt-pool, in the case of CGA, oxygen availability is too scarce for Cr oxidation and hence Cr diffuses out from the oxide. In the case of WA particulates, it is likely that they disperse into smaller oxide droplets under the influence of strong Marangoni-flows. Moreover, as oxygen availability is relatively high, Cr remains within the oxide. The following mechanism is therefore proposed: Surface oxide particulates melt together with the powder particles and under strong convective flows they disperse into nanometric droplets, hence no dissolution takes place. During the short interaction with the melt-pool, thermodynamic equilibrium is reached in the particles – which will be governed by the oxygen availability and the presence of strong oxide formers.
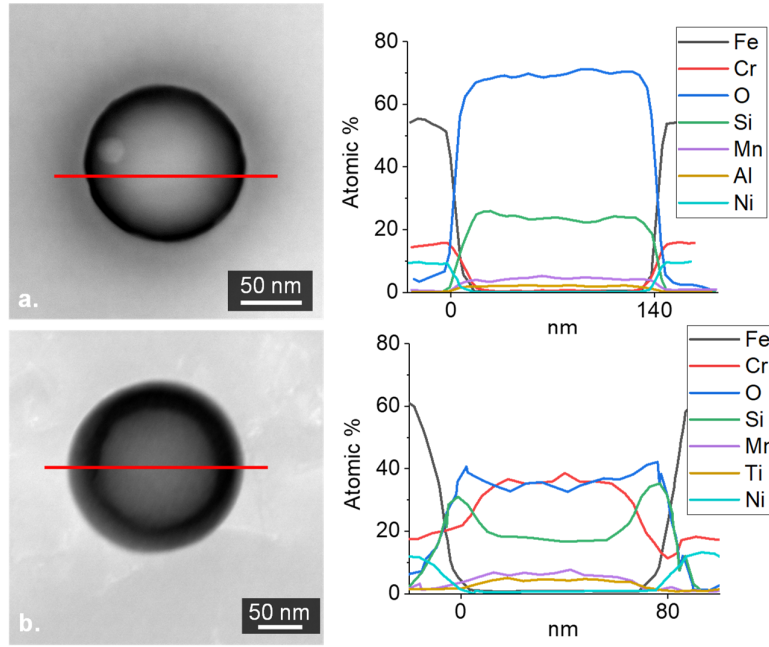
50

Figure 30. EDX line scans of oxides found in the a) CGA sample and b) WA sample.

Despite that there was no strong effect of the increased volume fraction of oxide dispersoids in the sample produced with WA powder, the concept of in-situ synthesis of ODS-like dispersoids was proven to work, resulting in a homogenous and nanometric dispersion of oxides within the microstructure at a higher volume fraction as compared to when using CGA powder.

Designing a Co-free stainless maraging steel for PBF-LB

As the in-situ synthesis of ODS stainless steels did not significantly alter the strength of the model alloy, another approach had to be taken. Consequently, the study presents a new Co-free stainless maraging variant for PBF-LB, developed using a computational design approach. The design goal was to approach the properties of the common maraging steel *18Ni300*, yet without any addition of Co and adding Cr for corrosion resistance. *18Ni300*, when processed with PBF-LB, can after aging reach hardness levels of 600 HV5 and a tensile strength of up to 2 GPa.

The modelling phase was initiated by establishing criteria that ensured corrosion resistance, good mechanical properties after aging, and high degree of printability. Based on the criteria and a general knowledge of similar alloy systems, a compositional range of the elements of interest was selected. To depict how the different ranges affected phase equilibria, calculations were made over the selected ranges and evaluated based on the set criteria. The candidates that fit the criteria underwent a detailed manual screening procedure to check for phase equilibria and precipitate fractions. Finally, the composition as shown in Table 3 was chosen, and its modelled precipitate is shown in Table 4.

Table 3. The designed composition of the investigated alloy.

Element	Cr	Ni	Al	Mo	Nb	Ti	Mn	Si	Fe
wt.%	13.2	9.1	1.1	0.6	0.5	0.23	0.5	0.5	Bal.
at.%	13.9	8.5	2.2	0.3	0.3	0.25	0.5	1	Bal.

Table 4. The calculated composition of the $L1_2$-Ni_3X precipitate that can form during aging.

	Ni	Al	Nb	Ti	Fe	Mn	Si	Cr
at.%	72	15.2	5	4.5	1.8	1.1	0.35	0.1

After powder atomization, the composition was printed using the parameter settings for *18Ni300.* The printing resulted in negligible residual porosity of <0.05%, without any cracks or other defects. Further investigations showed that the microstructure was fully martensitic with a hardness of 310 HV5. As retained austenite content was low, a direct-aging approach was chosen. The aging response as well as the results from the mechanical testing is presented in Figure 31. Peak hardness occurred at 18 h, with a value of 519 HV5. Hence, the designed composition showed rapid aging response – retaining relatively high hardness even after 90 h (where hardness dropped to 501 HV5).
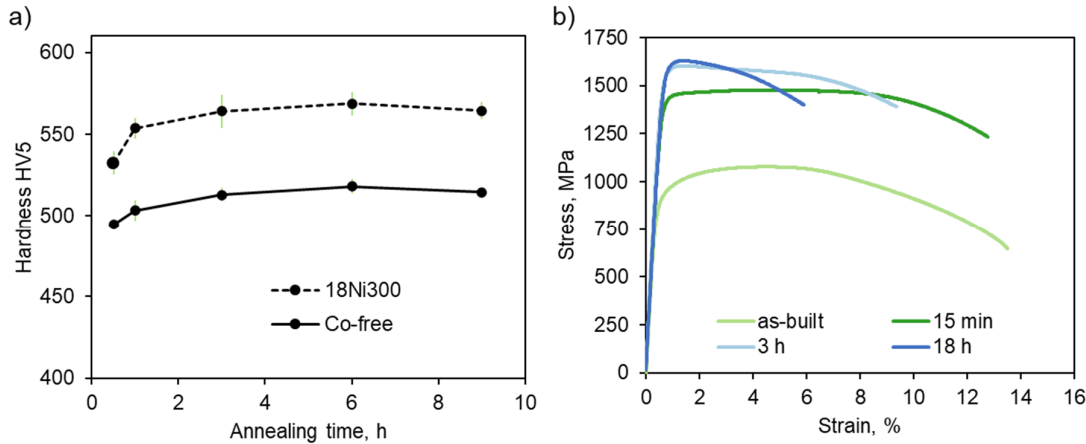

Figure 31. Mechanical properties of the Co-free maraging steel. a) the hardness response when aging at 500 °C, 18Ni300 is included for reference. b) tensile tests at various aging times when aged at 500 °C.

Atom probe investigations of the precipitates after 15 min of aging revealed high density, 1.5 x 10^{24} m^{-3}, of clusters rich in Ni, Al, Nb, Ti, Mn and Si. These clusters had an average radius of around 0.5 nm. After 3 h of aging, the clusters had evolved into more distinct precipitates, with an average radius of 1.4 nm. At this point, the average composition was 61Ni-24Al-4Nb-4Ti-2Mn-5Si. Following 18 h of aging, the precipitates underwent a complex splitting phenomenon, as shown in Figure 32. The splitting resulted in several precipitate types, including precipitates rich in Ni, Al, Mn and those rich in Ni, Ti, Nb, and Si. At this point, the total volume fraction of precipitates was 5.2%, with an average radius of 2 nm. Splitting of the precipitates resulted only in a shy increase of the hardness and strength of the alloy, while reducing the ductility significantly. For more balanced properties, the 3 h aged state would be preferred.
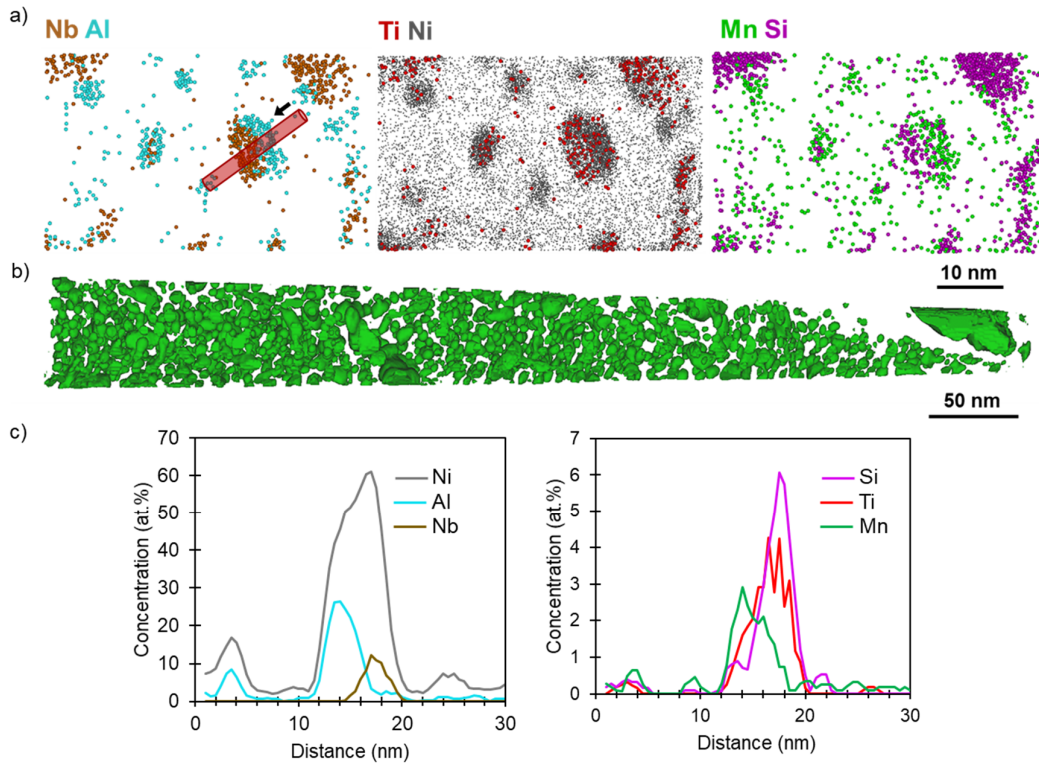
Figure 32. a) Atom maps from a 5 nm slice after 18 h of aging. b) Isosurfaces of Ni+Ti+Al+Nb (22at.%). c) 1D elemental profile of one of the split precipitates, diameter of the cylinder was 5 nm.

Overall, this investigation showed that it is possible to use computational alloy design to predict well-printable, directly hardenable, and coarsening resistant compositions for PBF-LB. Despite not fully reaching the properties of *18Ni300,* the investigated material exhibited very rapid precipitation resulting in high precipitate densities. Also, due to the splitting phenomenon the precipitates were found to resist coarsening very well.

8. Conclusions

With reference to the three major research questions (RQ1-RQ3), the important conclusions of this thesis study can be summarized as follows:

How do different atomization practices affect the powder and PBF-LB processability (RQ1)?

- Changing from argon to nitrogen gas atomization does not significantly affect the surface oxide state of 316L powder.
- The composition of powder surface oxide will largely depend on the oxygen affinity of the alloying elements.
- The presence of surplus oxygen originating from powder, such as WA powder, does not significantly affect PBF-LB processability.
- Drastic changes in the powder morphology, e.g., in the case of WA powder, severely affects flowability and the ability to reach high-powder packing.
- The changes in the flowability, and more importantly the packing efficiency, were shown to influence the printability of powder – especially at increasing layer thicknesses.

How are stainless steels strengthened through the PBF-LB process (RQ2)?

- The extensive thermo-mechanical cycling, inherent to the PBF-LB process, generates a cellular structure that effectively strengthens the alloy 316L.
- The cell walls are characterized by both thick dislocation networks and segregation and enrichment of primarily Cr and Mo, which provide a hindrance to dislocation glide yet allowing for cross-cellular slip. This results in local accumulation of strains at the cell walls.
- When heated to 800 °C, most of the elemental segregation is removed, leaving only a few dislocation tangles behind. Despite this, when mechanically loaded, local strains re-accumulate at the cell walls.
- The cellular structure lowers the strain hardening rate; hence neck formation occurs earlier with a lower total elongation to failure. Yet, the area reduction at the fracture point is equal, or greater, to when there is no cellular network.

How can the strength of stainless steels be increased without compromising processability (RQ3)?

- An increase in the volume fraction of oxide particles within PBF-LB processed alloy 316L did not cause an increase in strength. However, the concept of increasing the volume fraction by using WA powder was proven.
- The use of computational alloy design was shown to be successful in producing a precipitation hardened stainless steel for PBF-LB.
- The ductile martensitic matrix of this alloy ensured high PBF-LB processability while also keeping the precipitate forming elements in super-solution throughout the process.
- The precipitates gave rise to a 1.6 GPa tensile strength, nearly 1 GPa increase relative to the 316L alloy – while also displaying excellent temperature stability at elevated temperatures.

.

9. Future work

Based on the findings that are reported in this thesis, the published articles and numerous unpublished results, there are some topics that could benefit from further investigations. These are presented in further detail below.

Starting with the initial powder investigations, it would be beneficial to establish what elements or combination of thereof, pose a potential risk of being detrimental to the PBF-LB processability when atomized. For example, can certain powder surface oxides be linked to an increasing cracking susceptibility in stainless steels, which generally are considered quite robust. Continuing with powder surface oxides, further investigations into the carry-over mechanism of powder-to-part should be performed. As of now, a possible mechanism was proposed – however it was based on circumstantial post-mortem evidence and hence more direct observations would strengthen the hypothesis. Additionally, what are the governing factors to why some oxides are found in the microstructure with a spherical morphology, while other form thin films and cause cracks to form.

There is still quite some work remaining on the topic of relevant powder properties for AM. Despite the emergence of additional tools for powder characterization, most still lack a standardized testing procedure. Additionally, full measurement analysis of these systems should be performed, including inter-laboratory testing, to determine the capability and robustness of these systems. Looking at powder flowability in the context of printability, it would be beneficial to include powder grades that exhibit no Hall-flowability in trials such as those performed in *Paper II.* Typically, such powder batches show no significant signs of poor printability, as was indicated by preliminary trials. Yet, such batches often are scrapped when they fail the Hall-flowability tests. Therefore, it would be beneficial to characterize the flowability of such grades using alternative methods, to define the threshold point of no Hall-flowability and where such grades position themselves. Finally, it would be interesting to investigate the influence of faster re-coater speeds on the PBF-LB printability, especially at higher layer thicknesses. Through such investigations, perhaps we can get closer to defining the relevant powder properties for PBF-LB.

Regarding the strengthening mechanisms of PBF-LB processed 316L, although they have been extensively researched already, there are some remaining questions. One such question is how dislocations cross-slip between the cellular walls when the sample is mechanically loaded. Some researchers have indicated the formation of twins, or stacking faults, as dislocation pairs traverse cell walls and dissociate. Do these new interfaces provide further dislocation interactions? Therefore, a detailed TEM investigation of pre-strained samples would be interesting to conduct.

Finally, many of the precipitates in the developed maraging steel, as presented in *Paper V,* remain structurally uncharacterized. The structural determination can help both, in future simulations where such phases are better implemented into the databases of Thermo-Calc, and to get a better understanding of the how the precipitates develop during prolonged aging treatments. This kind of investigation is already underway, using synchrotron X-ray diffraction at the PETRA III beamline in Hamburg, Germany.

10. Acknowledgements

11.   References

[1]   M. Munsch, M. Schmidt-Lehr, E. Wycisk, and T. Führer, "Additive Manufacturing Market Report," AMPOWER, 2022.

[2]   "Evaluating the causes of cost reduction in photovoltaic modules," *Energy Policy*, vol. 123, pp. 700–710, Dec. 2018, doi: 10.1016/j.enpol.2018.08.015.

[3]   Y. M. Wang *et al.*, "Additively manufactured hierarchical stainless steels with high strength and ductility," *Nat. Mater.*, vol. 17, no. 1, pp. 63–71, Oct. 2017, doi: 10.1038/nmat5021.

[4]   A. Vance, "3-D Printing is Spurring a Manufacturing Revolution," *The New York Times*, Sep. 13, 2010. Accessed: Jan. 09, 2020. [Online]. Available: https://www.nytimes.com/2010/09/14/technology/14print.html

[5]   O. Andersson, A. Graichen, H. Brodin, and V. Navrotsky, "Developing Additive Manufacturing Technology for Burner Repair," *J. Eng. Gas Turbines Power*, vol. 139, no. 3, 2017, doi: 10.1115/1.4034235.

[6]   A. Frankel and A. Eckhoff, "Siemens: Digitalisation enables the industrialisation of metal AM," *Metal Additive Manufacturing*, vol. 4, no. 3, Sep. 01, 2018. Accessed: Jun. 16, 2022. [Online]. Available: https://www.metal-am.com/articles/siemens-digitalisation-enables-the-industrialisation-of-metal-3d-printing/

[7]   A. Palmquist, M. Jolic, E. Hryha, and F. A. Shah, "Complex geometry and integrated macro-porosity: Clinical applications of electron beam melting to fabricate bespoke bone-anchored implants," *Acta Biomater.*, Jun. 2022, doi: 10.1016/j.actbio.2022.06.002.

[8]   F42 Committee, "Terminology for Additive Manufacturing - General Principles - Terminology," ASTM International. doi: 10.1520/F3177-21.

[9]   M. Fousová, D. Vojtěch, K. Doubrava, M. Daniel, and C.-F. Lin, "Influence of Inherent Surface and Internal Defects on Mechanical Properties of Additively Manufactured Ti6Al4V Alloy: Comparison between Selective Laser Melting and Electron Beam Melting," *Materials*, vol. 11, no. 4, Art. no. 4, Apr. 2018, doi: 10.3390/ma11040537.

[10]   C. Körner, "Additive manufacturing of metallic components by selective electron beam melting — a review," *Int. Mater. Rev.*, vol. 61, no. 5, pp. 361–377, Jul. 2016, doi: 10.1080/09506608.2016.1176289.

[11]   J. Milberg and M. Sigl, "Electron beam sintering of metal powder," *Prod. Eng.*, vol. 2, no. 2, pp. 117–122, 2008.

[12]   T. DebRoy *et al.*, "Additive manufacturing of metallic components – Process, structure and properties," *Prog. Mater. Sci.*, vol. 92, no. Supplement C, pp. 112–224, Mar. 2018, doi: 10.1016/j.pmatsci.2017.10.001.

[13]   J. P. Oliveira, A. D. LaLonde, and J. Ma, "Processing parameters in laser powder bed fusion metal additive manufacturing," *Mater. Des.*, vol. 193, p. 108762, Aug. 2020, doi: 10.1016/j.matdes.2020.108762.

[14]   C. L. Druzgalski, A. Ashby, G. Guss, W. E. King, T. T. Roehling, and M. J. Matthews, "Process optimization of complex geometries using feed forward control for laser powder bed fusion additive manufacturing," *Addit. Manuf.*, vol. 34, p. 101169, Aug. 2020, doi: 10.1016/j.addma.2020.101169.

[15]   J. C. Fox, S. P. Moylan, and B. M. Lane, "Effect of Process Parameters on the Surface Roughness of Overhanging Structures in Laser Powder Bed Fusion Additive Manufacturing," *Procedia CIRP*, vol. 45, pp. 131–134, Jan. 2016, doi: 10.1016/j.procir.2016.02.347.

[16]   A. Leicht, M. Rashidi, U. Klement, and E. Hryha, "Effect of process parameters on the microstructure, tensile strength and productivity of 316L parts produced by laser powder

bed fusion," *Mater. Charact.*, vol. 159, p. 110016, Jan. 2020, doi: 10.1016/j.matchar.2019.110016.

[17] F. Calignano, G. Cattano, and D. Manfredi, "Manufacturing of thin wall structures in AlSi10Mg alloy by laser powder bed fusion through process parameters," *J. Mater. Process. Technol.*, vol. 255, pp. 773–783, May 2018, doi: 10.1016/j.jmatprotec.2018.01.029.

[18] A. Molinari *et al.*, "Effect of Process Parameters on the Surface Microgeometry of a Ti6Al4V Alloy Manufactured by Laser Powder Bed Fusion: 3D vs. 2D Characterization," *Metals*, vol. 12, no. 1, p. 106, Jan. 2022, doi: 10.3390/met12010106.

[19] M. Thomas, G. J. Baxter, and I. Todd, "Normalised model-based processing diagrams for additive layer manufacture of engineering alloys," *Acta Mater.*, vol. 108, pp. 26–35, Apr. 2016, doi: 10.1016/j.actamat.2016.02.025.

[20] J. C. Ion, H. R. Shercliff, and M. F. Ashby, "Diagrams for laser materials processing," *Acta Metall. Mater.*, vol. 40, no. 7, pp. 1539–1551, Jul. 1992, doi: 10.1016/0956-7151(92)90097-X.

[21] M. Attaran, "The rise of 3-D printing: The advantages of additive manufacturing over traditional manufacturing," *Bus. Horiz.*, vol. 60, no. 5, pp. 677–688, Sep. 2017, doi: 10.1016/j.bushor.2017.05.011.

[22] R. Poprawe, C. Hinke, W. Meiners, J. Schrage, S. Bremen, and S. Merkt, "SLM Production Systems: Recent Developments in Process Development, Machine Concepts and Component Design," in *Advances in Production Technology*, Cham, 2015, pp. 49–65. doi: 10.1007/978-3-319-12304-2_5.

[23] D. Buchbinder, H. Schleifenbaum, S. Heidrich, W. Meiners, and J. Bültmann, "High Power Selective Laser Melting (HP SLM) of Aluminum Parts," *Phys. Procedia*, vol. 12, no. Part A, pp. 271–278, Jan. 2011, doi: 10.1016/j.phpro.2011.03.035.

[24] C. Schwerz, F. Schulz, E. Natesan, and L. Nyborg, "Increasing productivity of laser powder bed fusion manufactured Hastelloy X through modification of process parameters," *J. Manuf. Process.*, vol. 78, pp. 231–241, Jun. 2022, doi: 10.1016/j.jmapro.2022.04.013.

[25] C. Schwerz, A. Raza, X. Lei, L. Nyborg, E. Hryha, and H. Wirdelius, "In-situ detection of redeposited spatter and its influence on the formation of internal flaws in laser powder bed fusion," *Addit. Manuf.*, vol. 47, p. 102370, Nov. 2021, doi: 10.1016/j.addma.2021.102370.

[26] C. Pauzon *et al.*, "Reduction of incandescent spatter with helium addition to the process gas during laser powder bed fusion of Ti-6Al-4V," *CIRP J. Manuf. Sci. Technol.*, vol. 35, pp. 371–378, Nov. 2021, doi: 10.1016/j.cirpj.2021.07.004.

[27] S. H. Luk, "Bulk Properties of Powders," in *Powder Metallurgy*, P. Samal and J. Newkirk, Eds. ASM International, 2015, pp. 111–126. doi: 10.31399/asm.hb.v07.a0006109.

[28] S. Vock, B. Klöden, A. Kirchner, T. Weißgärber, and B. Kieback, "Powders for powder bed fusion: a review," *Prog. Addit. Manuf.*, vol. 4, no. 4, pp. 383–397, Dec. 2019, doi: 10.1007/s40964-019-00078-6.

[29] ISO, "4490:2018: Metallic powders - Determination of flow rate by means of a calibrated funnel (Hall flowmeter)," International Organization for Standardization, Geneva, Switzerland, ISO Standard No. 4490, 2018. [Online]. Available: https://www.sis.se/produkter/metallurgi-dfbdd22b/pulvermetallurgi/ss-en-iso-44902018/

[30] F42 Committee, "Additive manufacturing Feedstock materials Methods to characterize metallic powders," ASTM International. doi: 10.1520/F3382-19.

[31] Y. Y. Sun, S. Gulizia, C. H. Oh, C. Doblin, Y. F. Yang, and M. Qian, "Manipulation and Characterization of a Novel Titanium Powder Precursor for Additive Manufacturing Applications," *JOM*, vol. 67, no. 3, pp. 564–572, Mar. 2015, doi: 10.1007/s11837-015-1301-3.

[32] J. A. Slotwinski and E. J. Garboczi, "Metrology Needs for Metal Additive Manufacturing Powders," *JOM*, vol. 67, no. 3, pp. 538–543, Mar. 2015, doi: 10.1007/s11837-014-1290-7.

[33] L. Cordova, T. Bor, M. de Smit, M. Campos, and T. Tinga, "Measuring the spreadability of pre-treated and moisturized powders for laser powder bed fusion," *Addit. Manuf.*, vol. 32, p. 101082, Mar. 2020, doi: 10.1016/j.addma.2020.101082.

[34] A. Strondl, O. Lyckfeldt, H. Brodin, and U. Ackelid, "Characterization and Control of Powder Properties for Additive Manufacturing," *JOM*, vol. 67, no. 3, pp. 549–554, Mar. 2015, doi: 10.1007/s11837-015-1304-0.

[35] L. P. Lefebvre, J. Whiting, B. Nijikovsky, S. E. Brika, H. Fayazfar, and O. Lyckfeldt, "Assessing the robustness of powder rheology and permeability measurements," *Addit. Manuf.*, vol. 35, p. 101203, Oct. 2020, doi: 10.1016/j.addma.2020.101203.

[36] D. Schulze, *Powders and Bulk Solids*. Berlin, Heidelberg: Springer Berlin Heidelberg, 2007. doi: 10.1007/978-3-540-73768-1.

[37] Z. Snow, R. Martukanitz, and S. Joshi, "On the development of powder spreadability metrics and feedstock requirements for powder bed fusion additive manufacturing," *Addit. Manuf.*, vol. 28, pp. 78–86, Aug. 2019, doi: 10.1016/j.addma.2019.04.017.

[38] A. Mussatto, R. Groarke, A. O'Neill, M. A. Obeidi, Y. Delaure, and D. Brabazon, "Influences of powder morphology and spreading parameters on the powder bed topography uniformity in powder bed fusion metal additive manufacturing," *Addit. Manuf.*, vol. 38, p. 101807, Feb. 2021, doi: 10.1016/j.addma.2020.101807.

[39] L. Marchetti and C. Hulme-Smith, "Flowability of steel and tool steel powders: A comparison between testing methods," *Powder Technol.*, vol. 384, pp. 402–413, May 2021, doi: 10.1016/j.powtec.2021.01.074.

[40] A. B. Spierings, M. Voegtlin, T. Bauer, and K. Wegener, "Powder flowability characterisation methodology for powder-bed-based metal additive manufacturing," *Prog. Addit. Manuf.*, vol. 1, no. 1–2, pp. 9–20, 2016.

[41] C. Pleass and S. Jothi, "Influence of powder characteristics and additive manufacturing process parameters on the microstructure and mechanical behaviour of Inconel 625 fabricated by Selective Laser Melting," *Addit. Manuf.*, vol. 24, pp. 419–431, Dec. 2018, doi: 10.1016/j.addma.2018.09.023.

[42] G. Yablokova *et al.*, "Rheological behavior of β-Ti and NiTi powders produced by atomization for SLM production of open porous orthopedic implants," *Powder Technol.*, vol. 283, pp. 199–209, Oct. 2015, doi: 10.1016/j.powtec.2015.05.015.

[43] A. T. Sutton, C. S. Kriewall, S. Karnati, M. C. Leu, and J. W. Newkirk, "Characterization of AISI 304L stainless steel powder recycled in the laser powder-bed fusion process," *Addit. Manuf.*, vol. 32, p. 100981, Mar. 2020, doi: 10.1016/j.addma.2019.100981.

[44] E. R. L. Espiritu, A. Kumar, A. Nommeots-Nomm, J. A. M. Lerma, and M. Brochu, "Investigation of the rotating drum technique to characterise powder flow in controlled and low pressure environments," *Powder Technol.*, vol. 366, pp. 925–937, Apr. 2020, doi: 10.1016/j.powtec.2020.03.029.

[45] L. Haferkamp, A. Spierings, M. Rusch, D. Jermann, M. A. Spurek, and K. Wegener, "Effect of Particle size of monomodal 316L powder on powder layer density in powder bed fusion," *Prog. Addit. Manuf.*, vol. 6, no. 3, pp. 367–374, Aug. 2021, doi: 10.1007/s40964-020-00152-4.

[46] P. Mellin, O. Lyckfeldt, P. Harlin, H. Brodin, H. Blom, and A. Strondl, "Evaluating flowability of additive manufacturing powders, using the Gustavsson flow meter," *Met. Powder Rep.*, vol. 72, no. 5, pp. 322–326, Sep. 2017, doi: 10.1016/j.mprp.2017.06.003.

[47] S. E. Brika, M. Letenneur, C. A. Dion, and V. Brailovski, "Influence of particle morphology and size distribution on the powder flowability and laser powder bed fusion manufacturability of Ti-6Al-4V alloy," *Addit. Manuf.*, vol. 31, p. 100929, Jan. 2020, doi: 10.1016/j.addma.2019.100929.

[48] K. Riener *et al.*, "Influence of particle size distribution and morphology on the properties of the powder feedstock as well as of AlSi10Mg parts produced by laser powder bed fusion (LPBF)," *Addit. Manuf.*, vol. 34, 2020, doi: 10.1016/j.addma.2020.101286.

[49] V. Seyda, D. Herzog, and C. Emmelmann, "Relationship between powder characteristics and part properties in laser beam melting of Ti–6Al–4V, and implications on quality," *J. Laser Appl.*, vol. 29, no. 2, p. 022311, May 2017, doi: 10.2351/1.4983240.

[50] A. Strondl, O. Lyckfeldt, H. Brodin, and U. Ackelid, "Characterization and Control of Powder Properties for Additive Manufacturing," *JOM*, vol. 67, no. 3, pp. 549–554, Mar. 2015, doi: 10.1007/s11837-015-1304-0.

[51] T. M. Wischeropp, C. Emmelmann, M. Brandt, and A. Pateras, "Measurement of actual powder layer height and packing density in a single layer in selective laser melting," *Addit. Manuf.*, vol. 28, pp. 176–183, Aug. 2019, doi: 10.1016/j.addma.2019.04.019.

[52] T. Liu *et al.*, "In-situ infrared thermographic inspection for local powder layer thickness measurement in laser powder bed fusion," *Addit. Manuf.*, vol. 55, p. 102873, Jul. 2022, doi: 10.1016/j.addma.2022.102873.

[53] A. Phua, P. S. Cook, C. H. J. Davies, and G. W. Delaney, "Powder spreading over realistic laser melted surfaces in metal additive manufacturing," *Addit. Manuf. Lett.*, vol. 3, p. 100039, Dec. 2022, doi: 10.1016/j.addlet.2022.100039.

[54] S. Hoeges, A. Zwiren, and C. Schade, "Additive manufacturing using water atomized steel powders," *Met. Powder Rep.*, vol. 72, no. 2, pp. 111–117, Mar. 2017, doi: 10.1016/j.mprp.2017.01.004.

[55] D. Riabov, L. Cordova, E. Hryha, and S. Bengtsson, "Effect of powder variability on laser powder bed fusion processing and properties of 316L," *Eur. J. Mater.*, vol. 2, no. 1, pp. 202–221, Dec. 2022, doi: 10.1080/26889277.2022.2064772.

[56] U. Scipioni Bertoli, G. Guss, S. Wu, M. J. Matthews, and J. M. Schoenung, "In-situ characterization of laser-powder interaction and cooling rates through high-speed imaging of powder bed fusion additive manufacturing," *Mater. Des.*, vol. 135, pp. 385–396, Dec. 2017, doi: 10.1016/j.matdes.2017.09.044.

[57] D. Bergström, J. Powell, and A. F. H. Kaplan, "The absorptance of steels to Nd:YLF and Nd:YAG laser light at room temperature," *Appl. Surf. Sci.*, vol. 253, no. 11, pp. 5017–5028, 2007, doi: https://doi.org/10.1016/j.apsusc.2006.11.018.

[58] P. Fischer, V. Romano, H. P. Weber, N. P. Karapatis, E. Boillat, and R. Glardon, "Sintering of commercially pure titanium powder with a Nd:YAG laser source," *Acta Mater.*, vol. 51, no. 6, pp. 1651–1662, Apr. 2003, doi: 10.1016/S1359-6454(02)00567-0.

[59] E. H. Amara and R. Fabbro, "Modelling of gas jet effect on the melt pool movements during deep penetration laser welding," *J. Phys. Appl. Phys.*, vol. 41, no. 5, p. 055503, Feb. 2008, doi: 10.1088/0022-3727/41/5/055503.

[60] T. Debroy and S. A. David, "Physical processes in fusion welding," *Rev. Mod. Phys.*, vol. 67, no. 1, pp. 85–112, 1995, doi: 10.1103/RevModPhys.67.85.

[61] A. F. H. Kaplan, "Fresnel absorption of 1μm- and 10μm-laser beams at the keyhole wall during laser beam welding: Comparison between smooth and wavy surfaces," *Appl. Surf. Sci.*, vol. 258, no. 8, pp. 3354–3363, Feb. 2012, doi: 10.1016/j.apsusc.2011.08.086.

[62]   K. C. Mills, B. J. Keene, R. F. Brooks, and A. Shirali, "Marangoni effects in welding," *Philos. Trans. R. Soc. Lond. Math. Phys. Eng. Sci.*, vol. 356, no. 1739, pp. 911–925, Apr. 1998, doi: 10.1098/rsta.1998.0196.

[63]   S. Ly, A. M. Rubenchik, S. A. Khairallah, G. Guss, and M. J. Matthews, "Metal vapor micro-jet controls material redistribution in laser powder bed fusion additive manufacturing," *Sci. Rep.*, vol. 7, no. 1, p. 4085, Jun. 2017, doi: 10.1038/s41598-017-04237-z.

[64]   N. Kouraytem *et al.*, "Effect of Laser-Matter Interaction on Molten Pool Flow and Keyhole Dynamics," *Phys. Rev. Appl.*, vol. 11, no. 6, p. 064054, Jun. 2019, doi: 10.1103/PhysRevApplied.11.064054.

[65]   P. Bidare, I. Bitharas, R. M. Ward, M. M. Attallah, and A. J. Moore, "Fluid and particle dynamics in laser powder bed fusion," *Acta Mater.*, vol. 142, pp. 107–120, Jan. 2018, doi: 10.1016/j.actamat.2017.09.051.

[66]   S. A. Khairallah, A. T. Anderson, A. Rubenchik, and W. E. King, "Laser powder-bed fusion additive manufacturing: Physics of complex melt flow and formation mechanisms of pores, spatter, and denudation zones," *Acta Mater.*, vol. 108, pp. 36–45, Apr. 2016, doi: 10.1016/j.actamat.2016.02.014.

[67]   M. J. Matthews, G. Guss, S. A. Khairallah, A. M. Rubenchik, P. J. Depond, and W. E. King, "Denudation of metal powder layers in laser powder bed fusion processes," *Acta Mater.*, vol. 114, pp. 33–42, Aug. 2016, doi: 10.1016/j.actamat.2016.05.017.

[68]   C. Pauzon *et al.*, "Effect of helium as process gas on laser powder bed fusion of Ti-6Al-4V studied with operando diffraction and radiography," *Eur. J. Mater.*, vol. 2, no. 1, pp. 422–435, Dec. 2022, doi: 10.1080/26889277.2022.2081622.

[69]   A. N. D. Gasper *et al.*, "Spatter and oxide formation in laser powder bed fusion of Inconel 718," *Addit. Manuf.*, vol. 24, pp. 446–456, Dec. 2018, doi: 10.1016/j.addma.2018.09.032.

[70]   C. Pauzon, A. Raza, E. Hryha, and P. Forêt, "Oxygen balance during laser powder bed fusion of Alloy 718," *Mater. Des.*, vol. 201, p. 109511, Mar. 2021, doi: 10.1016/j.matdes.2021.109511.

[71]   C. L. A. Leung, S. Marussi, R. C. Atwood, M. Towrie, P. J. Withers, and P. D. Lee, "In situ X-ray imaging of defect and molten pool dynamics in laser additive manufacturing," *Nat. Commun.*, vol. 9, no. 1, pp. 1–9, Apr. 2018, doi: 10.1038/s41467-018-03734-7.

[72]   A. J. Yule and J. J. Dunkley, *Atomization of Melts: For Powder Production and Spray Deposition*. Oxford : New York: Clarendon Press, 1994.

[73]   I. Campbell, O. Diegel, J. Kowen, and T. Wohlers, *Wohlers report 2018: 3D printing and additive manufacturing state of the industry: annual worldwide progress report*. Wohlers Associates, 2018.

[74]   S. Pleier, W. Goy, B. Schaub, M. Hohmann, M. Mede, and R. Schumann, "EIGA–an innovative production method for metal powder from reactive and refractory alloys," *Adv. Powder Metall. Part. Mater.*, 2004.

[75]   F. Proulx, C. A. D. Dion, and P. Carabin, "Method and apparatus for producing high purity spherical metallic powders at high production rates from one or two wires," WO2019232612A1, Dec. 12, 2019 Accessed: Sep. 30, 2020. [Online]. Available: https://patents.google.com/patent/WO2019232612A1/en?inventor=Christopher+Alex+Dorval+Dion&sort=new

[76]   M. Entezarian, F. Allaire, P. Tsantrizos, and R. A. L. Drew, "Plasma atomization: A new process for the production of fine, spherical powders," *JOM*, vol. 48, no. 6, pp. 53–55, Jun. 1996, doi: 10.1007/BF03222969.

[77]   C. A. D. DION, W. KREKLEWETZ, and P. Carabin, "Plasma apparatus for the production of high quality spherical powders at high capacity," WO2016191854A1, Dec.

08, 2016 Accessed: Sep. 30, 2020. [Online]. Available: https://patents.google.com/patent/WO2016191854A1/nl

[78] A. J. Heidloff *et al.*, "Advanced gas atomization processing for Ti and Ti alloy powder manufacturing," *JOM*, vol. 62, no. 5, pp. 35–41, May 2010, doi: 10.1007/s11837-010-0075-x.

[79] E. B. Pretorius and R. C. Nunnington, "Stainless steel slag fundamentals: from furnace to tundish," *Ironmak. Steelmak.*, vol. 29, no. 2, pp. 133–139, Apr. 2002, doi: 10.1179/030192302225003495.

[80] C. Choudhury and H. Kemmer, *Vacuum Melting and Remelting Processes*, Casting., vol. 15. ASM International, 1988. [Online]. Available: http://search.ebscohost.com/login.aspx?direct=true&AuthType=sso&db=cat07470a&A N=clc.96f1dbe5851c4c32b78372dc18b089c3&site=eds-live&scope=site&custid=s3911979&authtype=sso&group=main&profile=eds

[81] C. T. Sims, N. S. Stoloff, and W. C. Hagel, *Superalloys II*, 2nd ed. Wiley, 1987.

[82] I. E. Anderson, E. M. H. White, and R. Dehoff, "Feedstock powder processing research needs for additive manufacturing development," *Curr. Opin. Solid State Mater. Sci.*, vol. 22, no. 1, pp. 8–15, Feb. 2018, doi: 10.1016/j.cossms.2018.01.002.

[83] R. Ünal, "Improvements to close coupled gas atomisation nozzle for fine powder production," *Powder Metall.*, vol. 50, no. 1, pp. 66–71, Mar. 2007, doi: 10.1179/174329007X164899.

[84] C. F. Dixon, "Atomizing molten metals — a review," *Can. Metall. Q.*, vol. 12, no. 3, pp. 309–322, Jul. 1973, doi: 10.1179/cmq.1973.12.3.309.

[85] B. H. Rabin, G. R. Smolik, and G. E. Korth, "Characterization of entrapped gases in rapidly solidified powders," *Mater. Sci. Eng. A*, vol. 124, no. 1, pp. 1–7, Apr. 1990, doi: 10.1016/0921-5093(90)90328-Z.

[86] H. Franz, L. Plochl, and F.-P. Schimansky, "Recent advances of titanium alloy powder production by ceramic-free inert gas atomization," *Proc Titan.*, 2008.

[87] S. Spitans, H. Franz, and E. Baake, "Numerical Modeling and Optimization of Electrode Induction Melting for Inert Gas Atomization (EIGA)," *Metall. Mater. Trans. B*, vol. 51, no. 5, pp. 1918–1927, Oct. 2020, doi: 10.1007/s11663-020-01934-5.

[88] Y. Seki, S. Okamoto, H. Takigawa, and N. Kawai, "Effect of atomization variables on powder characteristics in the high-pressured water atomization process," *Met. Powder Rep.*, vol. 45, no. 1, pp. 38–40, Jan. 1990, doi: 10.1016/S0026-0657(10)80014-1.

[89] F. Persson, A. Eliasson, and P. Jönsson, "Prediction of particle size for water atomised metal powders: parameter study," *Powder Metall.*, vol. 55, no. 1, pp. 45–53, Feb. 2012, doi: 10.1179/1743290111Y.0000000016.

[90] T. Takeda *et al.*, "Method and apparatus for production of metal powder by atomizing," US6254661B1, Jul. 03, 2001 Accessed: Jan. 24, 2020. [Online]. Available: https://patents.google.com/patent/US6254661B1/en?inventor=Tokihiro+Shimura

[91] I. Olefjord and L. Nyborg, "Surface Analysis of Gas Atomized Ferritic Steel Powder," *Powder Metall.*, vol. 28, no. 4, pp. 237–243, Jan. 1985, doi: 10.1179/pom.1985.28.4.237.

[92] I. Olefjord and A. Nylund, "Surface reactions during rapid solidification and handling of Al5Mn2.5Cr powders," *Surf. Interface Anal.*, vol. 12, no. 7, pp. 401–406, 1988, doi: 10.1002/sia.740120707.

[93] L. Nyborg and I. Olefjord, "Surface Analysis of PM Martensitic Steel Before and After Consolidation: Part 1: Surface Analysis of Powder," *Powder Metall.*, vol. 31, no. 1, pp. 33–39, Jan. 1988, doi: 10.1179/pom.1988.31.1.33.

[94] T. Tunberg and L. Nyborg, "Surface Reactions During Water Atomisation and Sintering of Austenitic Stainless Steel Powder," *Powder Metall.*, vol. 38, no. 2, pp. 120–130, Jan. 1995, doi: 10.1179/pom.1995.38.2.120.

[95]   L. Nyborg, A. Nylund, and I. Olefjord, "Thickness determination of oxide layers on spherically-shaped metal powders by ESCA," *Surf. Interface Anal.*, vol. 12, no. 2, pp. 110–114, 1988, doi: 10.1002/sia.740120209.

[96]   M. Norell, L. Nyborg, and I. Olefjord, "Reactions during atomization of martensitic stainless steel," *Adv. Powder Metall.*, vol. 1, pp. 41–54, 1992.

[97]   L. Nyborg, M. Norell, and I. Olefjord, "Surface studies of powder metallurgical stainless steel," *Surf. Interface Anal.*, vol. 19, no. 1–12, pp. 607–614, 1992, doi: 10.1002/sia.7401901113.

[98]   I. Nyborg, T. Tunberg, and P. X. Wang, "Surface product formation during water atomization and sintering of austenitic stainless steel powder," *Met. Powder Rep.*, vol. 45, no. 11, pp. 750–753, Nov. 1990, doi: 10.1016/0026-0657(90)90459-T.

[99]   M. Vattur Sundaram, E. Hryha, D. Chasoglou, A. Rottstegge, and L. Nyborg, "Effect of Density and Processing Conditions on Oxide Transformations and Mechanical Properties in Cr–Mo-Alloyed PM steels," *Metall. Mater. Trans. A*, vol. 53, no. 2, pp. 640–652, Feb. 2022, doi: 10.1007/s11661-021-06539-4.

[100]   G. A. Rao, M. Srinivas, and D. S. Sarma, "Effect of oxygen content of powder on microstructure and mechanical properties of hot isostatically pressed superalloy Inconel 718," *Mater. Sci. Eng. A*, vol. 435, pp. 84–99, 2006, doi: 10.1016/j.msea.2006.07.053.

[101]   K. Saeidi, L. Kvetková, F. Lofaj, and Z. Shen, "Austenitic stainless steel strengthened by the in situ formation of oxide nanoinclusions," *RSC Adv.*, vol. 5, no. 27, pp. 20747–20750, Feb. 2015, doi: 10.1039/C4RA16721J.

[102]   H. Gruber, C. Luchian, E. Hryha, and L. Nyborg, "Effect of Powder Recycling on Defect Formation in Electron Beam Melted Alloy 718," *Metall. Mater. Trans. A*, vol. 51, no. 5, pp. 2430–2443, May 2020, doi: 10.1007/s11661-020-05674-8.

[103]   A. Raza *et al.*, "Degradation of AlSi10Mg powder during laser based powder bed fusion processing," *Mater. Des.*, vol. 198, p. 109358, Jan. 2021, doi: 10.1016/j.matdes.2020.109358.

[104]   T. Fiegl, M. Franke, A. Raza, E. Hryha, and C. Körner, "Effect of AlSi10Mg0.4 long-term reused powder in PBF-LB/M on the mechanical properties," *Mater. Des.*, vol. 212, p. 110176, Dec. 2021, doi: 10.1016/j.matdes.2021.110176.

[105]   J. R. Davis and ASM International, Eds., *Stainless steels*. Materials Park, Ohio: ASM International, 1994.

[106]   M. A. Meyers and K. K. Chawla, *Mechanical behavior of materials*, vol. 2. Cambridge University Press Cambridge, 2009.

[107]   W. O. Soboyejo, *Mechanical properties of engineered materials*. New York: Marcel Dekker, 2003.

[108]   A. H. Cottrell and B. A. Bilby, "Dislocation Theory of Yielding and Strain Ageing of Iron," *Proc. Phys. Soc. Sect. A*, vol. 62, no. 1, pp. 49–62, Jan. 1949, doi: 10.1088/0370-1298/62/1/308.

[109]   T. Gladman, I. D. McIvor, and F. B. Pickering, "Some aspects of the structure-property relationships in high-carbon ferrite-pearlite steels," *J Iron Steel Inst Lond.*, vol. 210, no. part 12, pp. 916–930, 1972.

[110]   H. Sieurin, J. Zander, and R. Sandström, "Modelling solid solution hardening in stainless steels," *Mater. Sci. Eng. A*, vol. 415, no. 1, pp. 66–71, Jan. 2006, doi: 10.1016/j.msea.2005.09.031.

[111]   J. Eliasson and R. Sandström, "Proof strength values for austenitic stainless steels at elevated temperatures," *Steel Res.*, vol. 71, no. 6–7, pp. 249–254, 2000, doi: 10.1002/srin.200001224.

[112] E. O. Hall, "The Deformation and Ageing of Mild Steel: III Discussion of Results," *Proc. Phys. Soc. Sect. B*, vol. 64, no. 9, pp. 747–753, Sep. 1951, doi: 10.1088/0370-1301/64/9/303.

[113] N. Petch, "The cleavage strength of polycrystals," *J. Iron Steel Inst.*, vol. 174, pp. 25–28, 1953.

[114] J. Li, "Fetch relation and grain boundary source," *Trans TMS-AIME*, vol. 227, pp. 239–242, 1963.

[115] M. A. Meyersm and E. Ashworth, "A model for the effect of grain size on the yield stress of metals," *Philos. Mag. A*, vol. 46, no. 5, pp. 737–759, Nov. 1982, doi: 10.1080/01418618208236928.

[116] H. Luo, X. Wang, Z. Liu, and Z. Yang, "Influence of refined hierarchical martensitic microstructures on yield strength and impact toughness of ultra-high strength stainless steel," *J. Mater. Sci. Technol.*, vol. 51, pp. 130–136, Aug. 2020, doi: 10.1016/j.jmst.2020.04.001.

[117] S. Morito, H. Yoshida, T. Maki, and X. Huang, "Effect of block size on the strength of lath martensite in low carbon steels," *Mater. Sci. Eng. A*, vol. 438–440, pp. 237–240, Nov. 2006, doi: 10.1016/j.msea.2005.12.048.

[118] K. M. Bertsch, G. Meric de Bellefon, B. Kuehl, and D. J. Thoma, "Origin of dislocation structures in an additively manufactured austenitic stainless steel 316L," *Acta Mater.*, vol. 199, pp. 19–33, Oct. 2020, doi: 10.1016/j.actamat.2020.07.063.

[119] A. J. Birnbaum, J. C. Steuben, E. J. Barrick, A. P. Iliopoulos, and J. G. Michopoulos, "Intrinsic strain aging, Σ3 boundaries, and origins of cellular substructure in additively manufactured 316L," *Addit. Manuf.*, vol. 29, p. 100784, Oct. 2019, doi: 10.1016/j.addma.2019.100784.

[120] G. Wang *et al.*, "The origin of high-density dislocations in additively manufactured metals," *Mater. Res. Lett.*, vol. 8, no. 8, pp. 283–290, Aug. 2020, doi: 10.1080/21663831.2020.1751739.

[121] L. Cui, S. Jiang, J. Xu, R. L. Peng, R. T. Mousavian, and J. Moverare, "Revealing relationships between microstructure and hardening nature of additively manufactured 316L stainless steel," *Mater. Des.*, vol. 198, p. 109385, Jan. 2021, doi: 10.1016/j.matdes.2020.109385.

[122] T. Voisin *et al.*, "New insights on cellular structures strengthening mechanisms and thermal stability of an austenitic stainless steel fabricated by laser powder-bed-fusion," *Acta Mater.*, vol. 203, p. 116476, Jan. 2021, doi: 10.1016/j.actamat.2020.11.018.

[123] T. Gladman, "Precipitation hardening in metals," *Mater. Sci. Technol.*, vol. 15, no. 1, pp. 30–36, Jan. 1999, doi: 10.1179/026708399773002782.

[124] E. Orowan, "Symposium on internal stresses in metals and alloys," *Inst. Met. Lond.*, vol. 451, 1948.

[125] A. J. Ardell, "Precipitation hardening," *Metall. Trans. A*, p. 35.

[126] D. Hull and D. J. Bacon, *Introduction to Dislocations*. Elsevier, 2011.

[127] E. Nembach, "Precipitation hardening caused by a difference in shear modulus between particle and matrix," *Phys. Status Solidi A*, vol. 78, no. 2, pp. 571–581, Aug. 1983, doi: 10.1002/pssa.2210780223.

[128] M. Ashby, "Oxide dispersion strengthening," in *AIME Conf. Proc., New York*, 1958, p. 143.

[129] R. L. Klueh, J. P. Shingledecker, R. W. Swindeman, and D. T. Hoelzer, "Oxide dispersion-strengthened steels: A comparison of some commercial and experimental alloys," *J. Nucl. Mater.*, vol. 341, no. 2–3, pp. 103–114, May 2005, doi: 10.1016/j.jnucmat.2005.01.017.

[130] M. Thuvander, M. Andersson, and K. Stiller, "Precipitation process of martensitic PH stainless steel Nanoflex," *Mater. Sci. Technol.*, vol. 28, no. 6, pp. 695–701, Jun. 2012, doi: 10.1179/1743284711Y.0000000115.

[131] M. K. Miller, E. A. Kenik, K. F. Russell, L. Heatherly, D. T. Hoelzer, and P. J. Maziasz, "Atom probe tomography of nanoscale particles in ODS ferritic alloys," *Mater. Sci. Eng. A*, vol. 353, no. 1–2, pp. 140–145, Jul. 2003, doi: 10.1016/S0921-5093(02)00680-9.

[132] I.-S. Kim *et al.*, "Defect and void evolution in oxide dispersion strengthened ferritic steels under 3.2 MeV Fe+ ion irradiation with simultaneous helium injection," *J. Nucl. Mater.*, vol. 280, no. 3, pp. 264–274, Aug. 2000, doi: 10.1016/S0022-3115(00)00066-0.

[133] M. J. Alinger, G. R. Odette, and D. T. Hoelzer, "On the role of alloy composition and processing parameters in nanocluster formation and dispersion strengthening in nanostuctured ferritic alloys," *Acta Mater.*, vol. 57, no. 2, pp. 392–406, Jan. 2009, doi: 10.1016/j.actamat.2008.09.025.

[134] S. J. Zinkle, "Fusion materials science: Overview of challenges and recent progress," *Phys. Plasmas*, vol. 12, no. 5, pp. 1–8, 2005, doi: 10.1063/1.1880013.

[135] S. Ukai, T. Kaito, S. Ohtsuka, T. Narita, M. Fujiwara, and T. Kobayashi, "Production and Properties of Nano-scale Oxide Dispersion Strengthened (ODS) 9Cr Martensitic Steel Claddings," *ISIJ Int.*, vol. 43, no. 12, pp. 2038–2045, 2003, doi: 10.2355/isijinternational.43.2038.

[136] S. Floreen, "The physical metallurgy of maraging steels," *Metall. Rev.*, vol. 13, no. 1, pp. 115–128, Jan. 1968, doi: 10.1179/mtlr.1968.13.1.115.

[137] P. Bajaj, A. Hariharan, A. Kini, P. Kürnsteiner, D. Raabe, and E. A. Jägle, "Steels in additive manufacturing: A review of their microstructure and properties," *Mater. Sci. Eng. A*, vol. 772, p. 138633, Jan. 2020, doi: 10.1016/j.msea.2019.138633.

[138] J. Schindelin *et al.*, "Fiji: an open-source platform for biological-image analysis," *Nat. Methods*, vol. 9, no. 7, Art. no. 7, Jul. 2012, doi: 10.1038/nmeth.2019.

[139] J. Goldstein *et al.*, *Scanning Electron Microscopy and X-Ray Microanalysis: A Text for Biologists, Materials Scientists, and Geologists*. Springer US, 1981. [Online]. Available: https://books.google.se/books?id=gwMUAQAAIAAJ

[140] E04 Committee, "Test Methods for Determining Average Grain Size," ASTM International. doi: 10.1520/E0112-13R21.

[141] S. I. Wright, M. M. Nowell, and D. P. Field, "A Review of Strain Analysis Using Electron Backscatter Diffraction," *Microsc. Microanal.*, vol. 17, no. 3, pp. 316–329, Jun. 2011, doi: 10.1017/S1431927611000055.

[142] F. Bachmann, R. Hielscher, and H. Schaeben, "Texture Analysis with MTEX – Free and Open Source Software Toolbox," *Solid State Phenom.*, vol. 160, pp. 63–68, 2010, doi: 10.4028/www.scientific.net/SSP.160.63.

[143] C. B. Carter and D. B. Williams, *Transmission electron microscopy: Diffraction, imaging, and spectrometry*. Springer, 2016.

[144] T. F. Kelly and M. K. Miller, "Atom probe tomography," *Rev. Sci. Instrum.*, vol. 78, no. 3, p. 031101, 2007.

[145] M. K. Miller, "Atom Probe Tomography and the Local Electrode Atom Probe," *Microsc. Microanal.*, vol. 10, no. S02, pp. 150–151, Aug. 2004, doi: 10.1017/S1431927604881157.

[146] M. K. Miller and R. G. Forbes, "The Local Electrode Atom Probe," in *Atom-Probe Tomography: The Local Electrode Atom Probe*, M. K. Miller and R. G. Forbes, Eds. Boston, MA: Springer US, 2014, pp. 229–258. doi: 10.1007/978-1-4899-7430-3_5.

[147] D. Vaumousse, A. Cerezo, and P. J. Warren, "A procedure for quantification of precipitate microstructures from three-dimensional atom probe data," *Ultramicroscopy*, vol. 95, pp. 215–221, May 2003, doi: 10.1016/S0304-3991(02)00319-4.

[148] D. Riabov, E. Hryha, M. Rashidi, S. Bengtsson, and L. Nyborg, "Effect of atomization on surface oxide composition in 316L stainless steel powders for additive manufacturing," *Surf. Interface Anal.*, vol. 52, no. 11, pp. 694–706, 2020, doi: 10.1002/sia.6846.

[149] D. Riabov, A. Leicht, J. Ahlström, and E. Hryha, "Investigation of the strengthening mechanism in 316L stainless steel produced with laser powder bed fusion," *Mater. Sci. Eng. A*, vol. 822, p. 141699, Aug. 2021, doi: 10.1016/j.msea.2021.141699.